WSS 80-20

WESTERN STATES SECTION

The Combustion Institute

1980 SPRING MEETING

21-22 APRIL 1980

THERMODYNAMIC ANALYSIS OF TURBULENT COMBUSTION IN A SPARK IGNITION ENGINE. EXPERIMENTAL EVIDENCE

G. P. Beretta
M. Rashidi
J. C. Keck

University of California

Irvine, California

Thermodynamic Analysis of Turbulent Combustion in a Spark Ignition Engine. Experimental Evidence

by

G.P. Beretta
M. Rashidi*
J.C. Keck

Department of Mechanical Engineering
Massachusetts Institute of Technology
Cambridge, MA. 02139

Presented at the Spring 1980 Meeting of the Western States Section
The Combustion Institute
April 21, 22, 1980
Irvine, California

Pages	21
Tables	7
Figures	15

*Present address: Mechanical Engineering Department, University of Technology, Tehran, Iran.

ABSTRACT

A method independent of physical modeling assumptions is presented to analyze high-speed flame photography and cylinder pressure measurements from a transparent-piston spark-ignition research engine. The method involves defining characteristic quantities of the phenomena of flame propagation and combustion, and estimating their values from the experimental information. Using only the pressure information, the mass fraction curves are examined. A new empirical burning law is presented which well simulates such curves. Statistical data for the characteristic delay and burning angles show that cycle-to-cycle fractional variations are of the same order of magnitude for both angles (about 20 percent). Using only the photographic information on flame front contours, statistics are obtained for the apparent true ignition delay time. Enflamed volume, area of the flame front and an average normal flame front speed are estimated as a function of time. From the combined analysis of cylinder pressure history and flame photography the entrainment speed u_e (often called turbulent flame speed) is estimated and found to increase rapidly during the initial period of flame propagation. At a later time, when the mass fraction burnt is greater than about five percent, u_e remains approximately constant at a value of the order of 10 m/s for the present operating conditions with cyclic fractional variations of about 20 percent. Comparison of the enflamed and burnt mass fractions indicates that a substantial amount of unburnt mass is inside the enflamed region during flame propagation. Comparison of the rates of entrainment and burning shows that the two processes are not coupled as it is implied when a thin flame is assumed. The characteristic burning time is found to be of the order of 1 ms and tends to decrease through the combustion period. The flame stretch factor is also estimated. The present work concentrates on experimental evidence which can be used to test theoretical models and computer simulations of the phenomenon.

1. INTRODUCTION

It is only in the last few years that the historically established empirical method of developing an internal combustion engine is being intensively and progressively complemented by the science of modelling. The reasons for this change are found in two main problems of the present society: the environmental problem, with the new constraints of strict emission standards, and the fuel shortage problem, with the consequent rising costs of the primary energy sources and the demand of more efficient use.

The empirical method of development cannot face, in an economic way, the complexity of the problem of optimizing efficiency at acceptable power levels subject to the new, rigid environmental and energy constraints. The present goal of the science of modelling is to provide a better analytical basis for such engine optimization effort. But there is also a less pragmatic reason that has received more and more attention in the history of the internal combustion engine: the need to understand the governing physical mechanisms of the processes occurring in a real operating engine.

The latter task is obviously of a great complication, since it involves going beyond the state of the art in all thermal sciences: non-equilibrium thermodyramics and chemical kinetics, unsteady fluid-dynamics and turbulence--all coupled in one problem.

A number of different approaches are being tried to tackle the modelling problem, and their success clearly depends on how the calculated results compare with experiments. The aim of the present work has been to extract experimental information on that small but important portion of the whole operating cycle of the spark-ignition engine where the combustion process takes place. This has been done by developing and applying a simple method to analyze the data generated by a non-conventional experiment--the non-conventional part

consisting in high-speed photography of flame propagation through a transparent piston in a single-cylinder, spark-ignition research engine.

It is well known that turbulence plays a fundamental role in the operation of a real engine. Mathematical theories have been proposed to deal with the turbulence problem [1 - 6], but no established physical description of a turbulent flow is yet available. The physics of turbulent flame propagation is even less understood [7-19]. For such reasons an attempt is made in this work to define quantities and obtain experimental estimates in a way which is independent of physical models of interpretation. The aim of this effort is to obtain experimental evidence against which the assumptions of any model of the phenomenon may be tested.

After a brief description of the experiment, a model independent method of analysis of the experimental data is presented and the results discussed. Consistent with the declared effort of the present work, physical interpretation of the results is left for future work.

2. EXPERIMENTAL APPARATUS AND MEASUREMENTS

The experiment was carried out on a transparent-piston engine [44]. Figure 1 shows an axial section of the cylinder-piston system which allows optical access to the combustion chamber through the quartz piston window. The cylinder head is a section of the head used by Ford on their 400 CID V-8 engine. Table 1 gives the details of the engine geometry and valve timing.

Because optical access is obtained through the piston, the original chamber and valve configuration could be conserved. The purpose of this experiment was to obtain detailed photographic information on the flame profiles through each cycle. High-speed photography was taken with a Hycam Model K-2001-R rotating-prism camera capable of taking up to five thousand frames

per second. In order to increase flame luminosity, the mixture of iso-octane and air was seeded with uniformly suspended salts, appropriately chosen not to affect flame propagation. The edge of the film was marked by a neon light pulse, synchronized to the flywheel, every twenty crank-angle degrees. Such markers provide a means to associate a crank angle to each frame of the photographic sequence.

The more conventional aspect of the experiment is the measurement of intake mass flow rates and of the cylinder pressure history. For the pressure measurement, the output of a piezoelectric transducer, suitably amplified, was A/D-converted by an on-line PDP 11 digital computer storing one pressure value every crank-angle degree.

The experimental procedure was the following: first, the engine was motored for a sufficiently long time to reach a complete steady state. Then, an electronic switching system was activated for the following sequence of operations: start the high-speed camera; wait for its speed to reach a threshold value; light the spark for ten to thirteen cycles, simultaneously activating the pressure data acquisition system.

As a result of this procedure the complete data set for each cycle of a sequence consists of the pressure measurement and the synchronized flame photographs as a function of crank-angle. Table 2 summarizes the operating conditions of the six sequences for which a complete data set was available.

Figure 2 shows a typical sequence of pressure traces as a function of crank angle for a sequence of 10 successive firing cycles. A consequence of the experimental procedure is that the first cycle of each sequence has no residual burnt fraction x_r and its pressure trace departs from the average.

Figure 3 shows a typical photographic sequence corresponding to pressure trace number 9 in Figure 2. The outer circular crown of the piston is used

to retain the quartz window (see Figure 1) and no direct photographic information on flame profiles is obtained in the corresponding corner region of the combustion chamber.

3. ANALYSIS OF EXPERIMENTAL DATA

3.1. Mass Fraction Burnt

Given a pressure measurement as a function of crank angle, a measure of inlet mass flow rates and an estimate of the residual burnt fraction x_r, the energy balance equation for the combustion chamber can be solved to yield the mass fraction burnt $x_b = m_b/m$ and all the other relevant thermodynamic properties of the gas mixture at each instant of time through the cycle. To perform this task, a version of the thermodynamic model presented by Tabaczynski, Ferguson and Radhakrishnan [20] was used. The estimate of heat losses was made following the correlation of Woshni [21] and crankcase blow-by was neglected.

From a different analytic version of the energy balance (Beretta [22]), it can be shown that neglecting blow-by will result in an underestimate (of the order of the blow-by itself) of the maximum value of x_b, $x_{b\ max}$. Given a pressure trace, many factors may influence the estimate of x_b and its maximum value, and they are all coupled in the energy balance equation. Underestimating heat losses, mass blow-by and pressure, results in underestimating x_b and $x_{b\ max}$. Underestimating inlet mass flow rates (i.e., the initial charge mass) results in overestimating x_b and $x_{b\ max}$.

Inlet mass flow rates were determined with a reasonable accuracy, and heat losses have a slight influence on $x_{b\ max}$. The problem of the dynamic calibration of the pressure transducer is, on the contrary, an important one. When the statically calibrated pressure trace was used to estimate x_b, low values of $x_{b\ max}$ were obtained (in the range 80 to 85 percent). To find what

reasonable value $x_{b\ max}$ should assume in our engine, the mass fraction quenched at the chamber walls was estimated to be about 1 percent of the charge mass (data from Ferguson and Keck [23] and Weiss [24] were used), the mass trapped in the piston crevice above the upper ring was about 4 percent, and a reasonable estimate of the blow-by underestimate was about 2 percent. The conclusion was that $x_{b\ max}$ should be around 93 percent. The disagreement was attributed to the calibration procedure, and it was decided to scale the pressure traces to obtain, on the average, the expected $x_{b\ max}$.

Obviously, having done this, a check had to be made on what is its influence on the subsequent analysis. When the results of the complete analysis for the same run, with and without a scaling factor of 10 percent were compared, the important quantities that will constitute the final results did not vary by the same amount as $x_{b\ max}$; namely, estimates of entrainment speed varied by a factor of 2 percent, well below the expected accuracy from such an experiment. Estimates of mass entrainment rate varied by less than 1 percent, while mass burning rates, as expected, varied by about the same 10 percent. Nonetheless, all trends and phase effects were conserved and we reached the conclusion that the scaling factor does not significantly affect the final results.

As a result of the thermodynamic analysis the following quantities of importance to the subsequent analysis are known as a function of crank-angle:

p, V, m	pressure, volume and total charge mass
ρ_u, $\dot{\rho}_u$, T_u	unburnt density, its time-derivative and unburnt gas temperature
x_b, $\dot{x}_b$, $\ddot{x}_b$	mass fraction burnt and its first and second time-derivatives

Figure 4 shows the normalized mass fraction burnt $\eta = x_b/x_{b\ max}$ vs. θ for the pressure curves in Figure 2.

In Figure 5, among other definitions, that of "burning angle" is visualized:

$$\Delta\theta_b = 6\ N \frac{x_{b\ max}}{\dot{x}_{b\ max}} \tag{1}$$

where N is the crankshaft speed (rev/min) and $\Delta\theta_b$ represents the number of crank-angle degrees that a line, tangent to the mass-fraction-burnt curve at the point of maximum slope, takes to rise from $x_b = 0$ to $x_b = x_{b\ max}$. The interval between spark and the angle at which the same line intersects $x_b = 0$ is called "delay angle", $\Delta\theta_d$. Table 3 shows the statistics of $\Delta\theta_d$, $\Delta\theta_b$ and $\Delta\theta_d + \Delta\theta_b$ for the analyzed sequences. Contrary to the common interpretation that the variations in delay angles are the main cause of cyclic variations, it is observed that the relative variations of both delay and burning angles are of the same order (about 20 percent). That positive variations of $\Delta\theta_d$ correlate to negative variations of $\Delta\theta_b$ can be inferred from the lower cyclic variations of the sum of the two angles.

3.1.1. Empirical burning law

In spite of the large cyclic variations in the mass-fraction-burnt curves, a remarkable stability is observed for the normalized plot of $\dot{x}_b/\dot{x}_{b\ max}$ vs. $x_b/x_{b\ max}$ presented in Figure 6 where the experimental curves for about seventy cycles have been superimposed.

It is found that the following family of curves well represents such behavior:

$$f(\eta) = C(a,b)\left[b\eta^{-a} + (1-b)(1-\eta)^{-a}\right]^{-1} \tag{2}$$

where

$\eta = x_b/x_{b\ max}$ = normalized mass fraction burnt

$f(\eta) = \dot{x}_b/\dot{x}_{b\ max} = \dot{\eta}\ x_{b\ max}/\dot{x}_{b\ max} = \dot{\eta}\Delta\theta_b/6N$

a = contact parameter

b = symmetry parameter

$$C(a,b) = b\left(1 + \left(\frac{1-b}{b}\right)^{1/1+a}\right)^{1+a} = \text{normalization factor}$$

$$\eta(f = 1) = \left(1 + \left(\frac{1-b}{b}\right)^{1/1+a}\right)^{-1} = \eta \text{ at the point of maximum slope}$$

Shown in the upper part of Figure 6 are plots of $f(\eta)$ vs η for $a = 0.84$ and $b = 0.45 \pm 0.10$, the value of the parameters best fitting the data of the lower part of the figure. Equation (2) is easily integrated to yield

$$\theta(\eta) - \theta_s = \frac{g(\eta)}{(1-a)\ C(a,b)}\ \Delta\theta_b \tag{3}$$

where θ_s is the crank-angle at spark and $g(\eta)$ is a dimensionless crank-angle (or time)

$$g(\eta) = b\eta^{1-a} - (1-b)(1-\eta)^{1-a} + 1 - b \tag{4}$$

Figure 7 shows the effect of parameters on the empirical burning law η vs $g(\eta)$.

The high degree of contact, presented by $g(\eta)$ after spark, is a characteristic that allows the use of θ_s as the spark crank angle. In the other existing empirical burning laws (Wiebe [25]; Blumberg and Kummer [26]), θ_s is not identified with the spark-angle, but as the point at which combustion begins, thus assigning to the ignition delay time a separate role, decoupled from flame propagation. This commonly accepted decoupling procedure is now believed not to represent the physics of the phenomenon. For example, Hires, Tabaczynski and Novak [27] have recognized, in their model, that the same mechanism should govern both delay and burning periods of combustion. Only,

due to the nature of turbulence and to variations in the mean flow field around the spark plug at spark time, the initial flame kernel may find a different geometrical and mean flow environment in which to develop.

Equation (4) makes it possible to link the values of all the intervals that can be defined on the mass-fraction-burnt curve, to the value of $\Delta\theta_b$ previously defined. With reference to Figure 5, the definitions of the other intervals are:

$$\Delta\theta_{0.1} = \theta(0.1) - \theta_s$$

$$\Delta\theta_d = \theta(\eta(f = 1)) - \theta_s - \frac{1}{2}\Delta\theta_b = \text{delay interval}$$

$$\Delta\theta_{0.1\text{-}0.9} = \theta(0.9) - \theta(0.1)$$

$$\Delta\theta_c = \theta(0.99) - \theta(0.01) = \text{combustion interval}$$

$$\Delta\theta_t \quad \theta(0.99) - \theta_s = \text{total combustion interval.}$$

In Table 4 the values of $\Delta\theta_d$, $\Delta\theta_b$, $\Delta\theta_{0.1}$, $\Delta\theta_{0.1\text{-}0.9}$ and $\Delta\theta_t$ are shown for the curves of Figure 4. In round brackets are their ratio to $\Delta\theta_b$. The ratio $\Delta\theta_t/\Delta\theta_b$, calculated from the burning law, is found to be very sensitive to the parameter a. For this reason it is kept fixed to the value 0.84 while the parameter b shown in Table 4 is calculated to match the experimental values of $\Delta\theta_d/\Delta\theta_b$. In square brackets are the corresponding predicted values for a = 0.84 and b = 0.42. For the given engine geometry, operating conditions and the case of edge ignition, the empirical burning law could be used to simulate cyclic variations by keeping the parameter a fixed and chosing the values of b and $\Delta\theta_b$ from Gaussians of given average and standard deviation (in our case both of the order of 20 percent).

3.2. Flame Front Geometry

In this work the flame front is operationally defined as the edge of the

photographic image on the film. Spatial averaging over small scale structure is already included due to the finite resolution of the system and line of sight integration of the exposing radiation. For each cycle of a sequence, the flame front profiles corresponding to each frame were superimposed on a drawing. The coordinates of the significative points for each flame contour were introduced in a digital computer for further automatic analysis as is shown in Figure 8a.

To obtain complete geometrical information on flame contours in the whole combustion chamber, assumptions are required to reconstruct the non-visible regions. The simplest reasonable assumption, generally consistent with observations [28], is to fit to the digitalized points of each flame front profile the best (least squares) circle, leaving as free parameters its radius r_f and the position x_c, y_c of its center. This assumption is clearly less restrictive than holding the center fixed at the spark location. Figure 8b shows the result of this procedure. The third dimension (i.e., the coordinate z_c of the best sphere) is assigned by assuming that the apparent flame center keeps the same relative distance from the cylinder head as the spark plug at spark time. Due to the high aspect ratio of the combustion chamber close to TDC, this assumption is not important.

A consistency check of our assumptions is obtained by following the path of the best center with time. During the early period of flame propagation, the center is found to move out from the spark plug, along a circular path on the x, y plane, at a velocity of about 1 m/s, consistently with the swirl velocity observed on the films at the end of combustion. At later times, the best center normally moves outward from such circular path, consistently with the fact that the flame front profiles become flatter.

Having r_f, x_c, y_c, z_c and knowing the geometry of the combustion chamber at the corresponding crank-angle, it is a geometrical problem to intersect the best sphere and the chamber geometry and obtain the shape of the enflamed region. The result is the estimate of the following parameters of the enflamed region, which are important in the subsequent analysis:

V_f volume of the enflamed region

$V_{\bar{f}}$, $\dot{V}_{\bar{f}}$ volume of the non-enflamed region ($V_f + V_{\bar{f}} = V$) and its time derivative

A_f area of the flame front

$A_{p\bar{f}}$ area of piston surface not yet interested by the flame

u_f average normal speed of the flame front.

A direct estimate of u_f is obtained dividing the average distance of two flame profiles by the time between the corresponding frames. An integral estimate of u_f is obtained from the knowledge of the above geometrical parameters of the enflamed region and the equation

$$\dot{V}_{\bar{f}} = -u_f A_f - u_p A_{p\bar{f}} \tag{5}$$

which defines the average normal speed u_f of the flame front.

Figure 9a shows the best flame front distance from the spark plug $r_f + x_c - x_s$ versus crank-angle θ for the typical cycle of Figure 8. Extrapolation at zero distance yields an apparent ignition crank-angle θ_i. Figure 9b shows direct and integral estimates of u_f; the remaining information in Figure 9 is discussed later.

3.3. Entrainment and Gas Speeds

Figure 10a shows cylinder head geometry and assumed spherical flame fronts for an early and a late visible contours. Figure 10b shows a plot of time versus flame front distance from spark. The average particle path is also indicated.

Assuming uniform pressure throughout the combustion chamber and negligible volume of the chemically reacting zones, the total mass m and volume V at any instant of time are given by

$$m = m_b + m_u \tag{6}$$

$$V = \frac{m_b}{\rho_b} + \frac{m_u}{\rho_u} \tag{7}$$

where ρ_b and ρ_u are spatially averaged densities of the burnt and unburnt gas mixtures.

With reference to Figure 10, we also have

$$m = m_f + m_{\bar{f}} = m_f + \rho_u V_{\bar{f}} \tag{8}$$

$$V = V_f + V_{\bar{f}} \tag{9}$$

where the subscripts f and $\bar{f}$ denote the volumes inside and outside the flame front. The entrainment speed u_e is defined as the average over the flame front surface of the normal component of the relative velocity at which unburnt gas mixture is entrained into the enflamed region

$$\rho_u A_f u_e = \dot{m}_f = -\dot{m}_{\bar{f}} = -\dot{\rho}_u V_{\bar{f}} - \rho_u \dot{V}_{\bar{f}} . \tag{10}$$

Similarly, the average normal component of the unburnt gas speed u_{gf} at the flame front is defined by

$$\rho_u A_f u_{gf} = \dot{m}_{\bar{f}}\Big|_{A_f} = \dot{\rho}_u V_{\bar{f}} - \rho_u A_{p\bar{f}} u_p \tag{11}$$

where u_p is the upward piston speed and the time derivative is taken for a control volume bounded by the cylinder walls, the moving piston face of area $A_{p\bar{f}}$ and a fixed surface just ahead of the flame front. Adding equations (10) and (11) and making use of equation (5) which defines the average normal speed u_f of the flame front, we obtain the familiar relation

$$u_e = u_f - u_{gf} \, . \tag{12}$$

The evaluation of u_e using equations (10) or (11) and (12) requires only the knowledge of $V_{\bar{f}}$, A_f and ρ_u as functions of time. From the analysis discussed in sections 3.1 and 3.2, we have an estimate for such quantities. In connection with the reliability of the estimate of u_e it is useful to investigate the behavior of u_{gf} at early times of flame propagation. Substituting equation (6) into (7), taking the time derivative and recalling that $\dot{V} = -A_p u_p$, we obtain

$$\frac{\dot{\rho}_u}{\rho_u} = \frac{\dot{m}_b}{\rho_u V}\left(\frac{\rho_u}{\rho_b} - 1\right) + \frac{m_b}{\rho_b V}\left(\frac{\dot{\rho}_u}{\rho_u} - \frac{\dot{\rho}_b}{\rho_b}\right) + \frac{A_p}{V} u_p \tag{13}$$

which substituted into (10) and (11) yields alternative expressions for u_e and u_{gf}. At early times, when the flame has not yet hit the piston face, $A_{p\bar{f}} = A_p$ and it is reasonable to assume $\dot{\rho}_b/\rho_b \approx \dot{\rho}_u/\rho_u$ and $V_{\bar{f}} \approx V$ to obtain

$$u_{gf} \approx \frac{\dot{m}_b}{\rho_u A_f}\left(\frac{\rho_u}{\rho_b} - 1\right). \tag{14}$$

Since u_f and u_{gf} are determined independently, the fractional error in u_{gf} and u_e can be estimated from the relations

$$\left(\frac{\delta u_{gf}}{u_{gf}}\right)^2 = \left(\frac{\delta \dot{x}_b}{\dot{x}_b}\right)^2 + \left(\frac{\delta A_f}{A_f}\right)^2 \tag{15a}$$

and

$$\frac{\delta u_e}{u_e} = \frac{((\delta u_f)^2 + (\delta u_{gf})^2)^{1/2}}{u_f - u_{gf}} \tag{15b}$$

where the errors in ρ_u and ρ_b are assumed to be negligible. When the flame front first becomes visible, its radius is approximately 5 mm and the mass fraction burnt $x_b \sim 0.001$ and its time derivative is essentially unmeasurable. Thus at early times the errors in u_e and u_{gf} are due entirely to the errors in $\dot{x}_b$ which, in practice, are large for $x_b \leq 0.05$. Nevertheless, a tentative estimate of u_e at early times is obtained from Figure 9b where u_f and u_{gf} are plotted for the typical cycle. The difference between the two curves yields the value of u_e, plotted in Figure 9c versus θ, corresponding to the integral and direct estimates of u_f. When $x_b \geq 0.05$, such an estimate is reliable and in Figure 11 the mean values of u_e are determined for two typical runs. When $x_b \leq 0.05$, the reliability is weak as discussed above. The tendency of u_e to start from a low value (close to the value of the laminar flame speed S_ℓ), then rapidly increase during the early period of combustion and eventually remain approximately constant for the remaining time is in agreement with the prediction of the rapid distortion theory (Wong and Hoult [29]).

Table 5 shows the statistics of $\bar{u}_e$ (average for $x_b > 0.05$), $u_b = (R - x_s)6N/\Delta\theta_b$, $\tau_d = \Delta\theta_d/6N$ and the apparent ignition delay time $\tau_i = (\theta_i - \theta_s)/6N$ where θ_i is defined in Figure 9a. No strong correlation is observed between $\bar{u}_e$ and u_b. Figure 12 shows the expected scaling of $\bar{u}_e$ with engine speed.

3.4. Comparison of Enflamed and Burnt Mass Fractions and of Entrainment and Burning Rates

The observation that for $x_b > 0.05$ the entrainment speed u_e does not show either increasing or decreasing trends is used to reconstruct flame front geometry in the non-visible region beyond the window edge. The dashed curve in Figure 9b is used to interpolate between the observed values of u_f and the limiting value of $u_f = u_e$ when the gas is fully entrained and $u_{gf} = 0$. Knowing V_f at any instant of time, the mass fraction enflamed $x_f = m_f/m$ can be estimated from equation (8) and normalized curves versus crank-angle for the sequence of Figure 4 are shown in Figure 13. It is observed that the mass fraction burnt curves are delayed with respect to the mass fraction enflamed curves of about 10 crank-angle degrees. Figure 14 shows normalized plots of x_f vs. x_b for the same sequence. A significant amount of unburnt mass is observed inside the enflamed region (e.g., for the average cycle when $x_f = 0.6$ we read $x_b \sim 0.3$).

Figure 15a shows plots of normalized entrainment rate $\dot{x}_f/\dot{x}_{b\ max}$, burning rate $\dot{x}_b/\dot{x}_{b\ max}$ and $\ddot{x}_b/\dot{x}_{b\ max}$ as a function of $x_b/x_{b\ max}$ for the typical cycle. The importance of these plots is that they prove that the entrainment and burning processes are decoupled and thin flame assumptions cannot incorporate this experimental evidence. It is suggested that such plots be considered as important tests of turbulent flame propagation models.

3.4.1. Characteristic burning time

A characteristic burning time τ can be defined as the instantaneous mean life time of an unburnt fluid particle in the enflamed region by the relation

$$\tau \dot{x}_b = x_f - x_b \ . \tag{16}$$

To evaluate τ from the available experimental information, either equation (16)

can be used or its time derivative

$$\tau \ddot{x}_b = \dot{x}_f - \dot{x}_b(1 + \dot{\tau}) \tag{17}$$

where the value for $\dot{\tau}$ can be estimated from the result of equation (16) (when $x_b \geq 0.2$ we find $\dot{\tau} \sim -0.2$).

Figure 15b shows normalized plots of $x_f - x_b$ and $\dot{x}_f - \dot{x}_b$. By inspection of Figures 15a and 15b and using equations (16) and (17), both estimates of the value of τ are shown in Figure 15c for the typical cycle. τ is of order of 1 ms and after an early increase it shows a permanent decreasing trend.

The notion of a characteristic burning time τ was first introduced by Blizard and Keck [30]. It is to be noted that in the present work no use has been made of physical modeling interpretations of the analyzed phenomenon.

3.4.2. Flame stretch factor

At given thermodynamic conditions the values of the laminar flame speed S_ℓ are available from experimental measurements (e.g., Metghalchi and Keck [31]). Therefore, an equivalent laminar flame front area A_b can be defined by the relation

$$\rho_u A_b S_\ell = \dot{m}_b \tag{18}$$

Equation (18) substituted into (14) yields

$$u_{gf} \approx S_\ell \frac{A_b}{A_f} \left| \frac{\rho_u}{\rho_b} - 1 \right| \tag{19}$$

where the term A_b/A_f is defined in the literature [32-35] as the flame stretch factor. Its estimate by using equation (18) is shown in Figure 9b. Also shown are the theoretical values at which the quantities shown would tend in the limit as $r_f \to 0$ at $\theta = \theta_i$ if it is assumed $A_b/A_f \to 1$ and $u_e \to S_\ell$, i.e.,

$$u_{gf} \rightarrow u_2 = S_\ell \left(\frac{\rho_u}{\rho_b} - 1 \right) \tag{20a}$$

$$u_f \rightarrow u_1 = S_\ell \frac{\rho_u}{\rho_b} \tag{20b}$$

where u_1 and u_2 are the familiar relations of laminar flame propagation at constant pressure. The data would better agree with the assumption, say, of $A_b/A_f \rightarrow 1.5\text{-}2.0$ as $r_f \rightarrow 0$.

4. DISCUSSION AND CONCLUSIONS

4.1. Previous Works

As we repeatedly said, no physical modeling assumptions or interpretations have been used so far in the analysis of the experimental information. This is of fundamental importance for the results to be considered in testing physical models and computer simulations of turbulent flame propagation in a spark-ignition engine.

Blizard and Keck [30] have estimated u_e using ionization probes in the place of photography. They obtained an average value of u_e during a cycle, determined by assuming: (1) spherical flame geometry, centered at the spark plug; (2) an exponential distribution of burning times for the entrained eddies; and (3) constant u_e along the cycle. A comparison of their results with the present estimates is given in Table 6. In their modeling work, Blizard and Keck defined a laminar burning length scale by the relation

$$\ell_\ell = \tau S_\ell \tag{21}$$

interpreting it as the characteristic size of laminar subregions or "eddies" of the turbulent flow field which immediately start burning after entrainment at the laminar flame speed. A similar interpretation is given in flame

stretching theories [32-35] for the equivalent laminar flame front area A_b as the total area of the extremely thin, highly convoluted laminar flame front contained within the turbulent burning zone behind the turbulent flame front.

Lancaster, et al. [36] attempted to estimate u_e from the thermodynamic information only. In fact, they estimated an equivalent thin-flame entrainment speed which is a good estimate only during the central period of combustion (around $\ddot{x}_b = 0$). During the central period, using measured values of the turbulence intensity u' [37], they could correlate the values of u', u_e and S_ℓ for different operating conditions.

The value of u_e, in the literature more often called turbulent flame speed, has been related in a variety of ways to the turbulence intensity u' and the laminar flame speed S_ℓ. This literature has been reviewed recently by Andrews, Bradley and Lwakabamba [38]. The most used relations are those found in [7-10]. A common feature of all of them is a direct dependence of u_e on u'; i.e., if u' increases, u_e also increases. The difference between various models is in the nature of such dependence.

Experimental measures of turbulence intensity and structure in the combustion chamber of an S.I. engine have also been presented in the literature [37, 39-43]. However, such measures, of fundamental importance to understand the role of turbulence in the mechanisms of flame propagation, are very critical and of difficult correct interpretation. A typical value of u', for operating conditions similar to the present and arount TDC, is of the order of 10 m/s, i.e., of the same order as u_e.

4.2. Conclusions

An experiment was carried out on a transparent-piston spark-ignition engine to obtain high-speed flame photography and cylinder pressure

measurements of the turbulent flame propagation and combustion period of an engine operating cycle.

1. From the thermodynamic analysis of the pressure measurements only, data for cycle-to-cycle variations of both delay and burning angles are found to be of the same order of magnitude (about 20 percent).
2. A new two-parameter empirical burning law, of practical usefulness in first-order computer simulations of engine operating cycles, has been presented and compared to experimental results. Its advantage is that it starts at spark and can simulate both delay and burning periods. Its application to simulate cyclic variations has been suggested.
3. A model independent method to analyze the combined photographic and pressure information is presented. Its importance is that the present results can be used to test physical modeling assumptions and the results of computer solutions of the flow field equations.
4. The method is based on the definition of the entrainment speed u_e, the unburnt gas speed at the flame front u_{gf}, and the flame front speed u_f in terms of quantities that can be estimated from the experimental data.
5. Estimated values of u_e tend to increase rapidly in the early period of flame propagation until the mass fraction burnt is $x_b \approx 0.05\text{-}0.10$. Then u_e remains approximately constant through the rest of the period. Its absolute value for the present engine operating conditions is about 10 m/s with cycle-to-cycle variations of the order of 20 percent.
6. Enflamed and burnt mass-fraction curves are compared through the single cycle and a substantial fraction of the enflamed mass is found to be unburnt. Thin-flame models cannot incorporate this observation.

7. Entrainment and burning rate curves are compared and the result proves that the two processes are decoupled.
8. A characteristic burning time τ is defined and found to assume values about 1 ms with a tendency to decrease during the combustion period. A flame stretch factor A_b/A_f is defined and estimated from experimental data.

APPENDIX: CHARACTERISTIC LENGTH SCALES

To help the physical interpretation of the present results, Table A shows a summary of characteristic length scales of the turbulent reacting flow field inside the combustion chamber. Columns a and b refer to the beginning and the end of a typical cycle. Following the relations reviewed by Andrews, et al. [38], we recall the expressions for Taylor and Kolmogorov microscales:

$$\lambda = \ell\, C^{1/2}\, Re_\ell^{-1/2} \tag{A.1}$$

$$\eta = \lambda\, 15^{-1/4}\, Re_\lambda^{-1/2} \tag{A.2}$$

where

ℓ = integral length scale (assumed equal to the instantaneous clearance height)

$C \simeq 48$ (experimental constant for isotropic turbulence)

$Re_\ell = \frac{u'\ell}{\nu}$ = turbulent Reynolds number

$Re_\lambda = \frac{u'\lambda}{\nu}$ = microscale Reynolds number

u' = turbulence intensity (assumed $\sim u_e \sim 10$ m/s)

ν = kinematic viscosity.

$\ell_f = \tau u_e$ can be interpreted as a characteristic turbulent flame thickness.

A diffusion length over the compression stroke is calculated from the relation $\delta = \sqrt{\nu \bar{t}}$, where $\bar{t}$ is the time from inlet valve closes.

An estimate of the laminar flame thickness, $\delta_\ell \sim k/(\rho_u S_\ell c_p)$, where k is the thermal conductivity, is also tabulated. δ_q is the value of the wall quench distance [23-24].

ACKNOWLEDGMENTS

It is a pleasure to thank Professor John B. Heywood for his invaluable critical help during the course of this work.

The work was supported by NASA under Grant Number NSG-3245.

REFERENCES

1. Batchelor, G.K., The Theory of Homogenous Turbulence, Cambridge University Press, Great Britain (1954).
2. Orszag, S.A., J. Fluid Mechanics 41, 363-386 (1970).
3. Townsend, A.A., J. Fluid Mechanics 41, 13-46 (1970).
4. Launder, B.E. and Spalding, D.B., Mathematical Model Academic Press, London (1972).
5. Tennekes, H. and Lumley, J.L., A First Course in Turbulence, The M.I.T. Press, Cambridge, Massachusetts (1972).
6. Pope, S.B., Phil. Trans. R. Soc. Lond. 291, 529-568 (1979).
7. Damköhler, G., Z. Elektrochemie Angewandte Physikalische Chemie 46, 601-626 (1940). (English translation, NACA TM 1112 (1947)).
8. Shelkin, K.I., Jour. Tech. Phys. (USSR) 13, 520-530 (1943). (English translation, NACA TM 1110 (1947)).
9. Leason, D.B., Fuel 30, 233 (1951).
10. Karlovitz, B., Fourth Symposium (International) on Combustion, Williams and Wilkins, Baltimore, 60-67 (1953).
11. Shchetinkov, E.S., Combustion in Turbulent Flow (L.N. Khitrin, Ed.), Moscow (1959). (English translation, IPST (1963), 1-40.)
12. Vlasov, K.P., in Combustion in Turbulent Flow (L.N. Khitrin, Ed.), Moscow (1959). (English translation, IPST (1963), 41-47.)
13. Sokolik, A.S., in Combustion in Turbulent Flow (L.N. Khitrin, Ed.), Moscow (1959). (English translation, IPST (1963), 52-67.)
14. Semenov, E.S., in Combustion in Turbulent Flow (L.N. Khitrin, Ed.), Moscow (1959). (English translation, IPST (1963), 123-147.)

15. Chomiak, J., Combustion and Flame 15, 319-321 (1970).

16. Spalding, D.B., in Thirteenth Symposium (International) on Combustion, The Combustion Institute, 649-567 (1971).

17. Chomiak, J., in Sixteenth Symposium (International) on Combustion, The Combustion Institute, 1665-1672 (1976).

18. Spalding, D.B., Combustion Science and Technology 13, 3-22 (1976).

19. Tabaczynski, R.J., Prog. Energy Combust. Sci. 2, 143-165 (1976).

20. Tabaczynski, R.J., Ferguson, C.R. and Radhakrishnan, K., SAE Paper 770647 (1977).

21. Woschni, G., SAE Paper 670931 (1967).

22. Beretta, G.P., M.Sc. Thesis, Part II, 89-115, M.I.T., Cambridge, Mass. (1980).

23. Ferguson, C.R. and Keck, J.C., Combustion and Flame 28, 197-205 (1977).

24. Weiss, P., M.Sc. Thesis, M.I.T., Cambridge, Mass. (1980).

25. Wiebe, J.J., Kraftadrzeugtechnik 9, translated by Prof. A. Joute and T.H. Dresen (1960).

26. Blumberg, P. and Kummer, J.T., Combustion Science and Technology 4, 73-95 (1971).

27. Hires, S.D., Tabaczynski, R.J. and Novak, J.M., SAE Paper 780232 (1978).

28. Namazian, M., Hansen, S., Lyford-Pike, E., Sanchez-Barsse, J., Heywood, J.B. and Rife, J., SAE Paper 800044 (1980).

29. Wong, V.W. and Hoult, D.P., SAE Paper 790357 (1979).

30. Blizard, N.C. and Keck, J.C., SAE Paper 740191 (1974).

31. Metghalchi, H., Ph.D. Thesis, M.I.T., Cambridge, Mass. (1980).

32. Karlovitz, B., Denniston, D.W., Jr., Knapschaefer, D.H. and Wells, F.E., Fourth Symposium (International) on Combustion, Williams and Wilkins, Baltimore, 613 (1953).

33. Lewis, B. and von Elbe, G., Combustion, Flames and Explosions of Gases, Academic Press, London (1961), p. 336.

34. Reed, S.B., Combustion and Flame 11, 177 (1967).

35. Thomas, A., Report CUEDIA - Thermo 1TR.10, Department of Engineering, Cambridge University, England (1979).

36. Lancaster, D.R., Krieger, R.B., Sorenson, S.C. and Hull, W.L., SAE Paper 760160 (1976).

37. Lancaster, D.R., SAE Paper 760159 (1976).

38. Andrews, G.E., Bradley, D. and Lwakabamba, S.B., Combustion and Flame 24, 285-304 (1975).

39. Tsuge, B.M., Kido, H. and Yanagihara, H., Bull. of the JSME 16, 244-251 (1973).

40. Tsuge, B.M., Kido, H. Kato, K. and Nomiyama, Y., Bull. of the JSME 17, 587-594 (1974).

41. James, E.H. and Lucas, G.G., SAE Paper 750885 (1975).

42. Dent, J.C. and Salama, N.S., SAE Paper 750886 (1975).

43. Witze, P.O., SAE Paper 770220 (1977).

44. Rashidi, M., to be published in Proc. Inst. Mech. Eng.

List of Tables

TABLE 1. Engine parameters

Compression ratio	CR	7.86
Bore, mm	b	101.6
Stroke, mm	S	88.9
Clearance height, mm	h	13.0
Equivalent wedge angle, rad	α	0.17
Spark plug distance from center, mm	x_s	-29.5
Inlet port diameter, mm	D	48.3
Inlet valve lift, mm	L	9.3
Inlet valve opens, deg. ATDC	IVO	-410^o
Inlet valve closes, deg. ATDC	IVC	-140^o
Exhaust valve opens, deg. ATDC	EVO	$+130^o$
Exhaust valve closes, deg. ATDC	EVC	$+390^o$
Spark advance, deg. BTDC	SA	30^o
Throttle, wide open	WOT	
Fuel, iso-octane	C_8H_{18}	
Fuel-air equivalence ratio	ϕ	1.0 - 1.2
Crankshaft speed, rev/min	N	900 - 1200

TABLE 2. Test matrix*

Run No.	N	ϕ
1	870	1.09
2	1045	1.00
3	1100	1.14
4	1120	1.07
5	1220	1.14
6	1230	1.07

N = Engine speed, rev/min

Φ = Fuel-air equivalence ratio

TABLE 3. Statistics of $\Delta\theta_d$, $\Delta\theta_b$ and $\Delta\theta_d + \Delta\theta_b$ for the analyzed sequences

Run No.		Cycle No.														
		2	3	4	5	6	7	8	9	10	11	12	13	Avg	Rel. Var.	First Cycle
1	$\Delta\theta_d$	20.0	22.0	19.1	22.7	20.4	15.1	18.5	21.8	19.6	-	-	-	19.9	12%	11.9
	$\Delta\theta_b$	24.0	19.9	17.8	22.6	19.3	25.8	23.0	28.3	20.8	-	-	-	22.4	14%	20.3
	+	44.0	41.9	36.9	45.3	39.7	40.9	41.5	50.1	40.4	-	-	-	42.3	9%	32.2
2	$\Delta\theta_d$	25.2	25.9	33.8	25.3	32.5	24.3	28.8	28.3	22.1	-	-	-	27.4	14%	16.4
	$\Delta\theta_b$	33.5	24.1	24.4	29.3	35.0	35.5	22.4	23.4	27.7	-	-	-	28.4	17%	23.2
	+	58.7	50.0	58.2	54.6	67.5	59.8	51.2	50.7	49.8	-	-	-	55.6	11%	39.6
3	$\Delta\theta_d$	20.9	20.5	19.1	20.8	19.0	24.9	28.1	32.4	20.0	-	-	-	22.9	20%	20.9
	$\Delta\theta_b$	18.2	23.0	29.9	18.4	21.9	22.3	27.8	23.1	24.1	-	-	-	22.6	16%	22.2
	+	39.1	43.5	49.0	39.2	40.9	47.2	55.9	55.5	44.1	-	-	-	46.0	14%	43.1
4	$\Delta\theta_d$	24.8	18.7	20.7	23.3	23.0	25.8	16.8	24.7	22.2	22.6	17.5	-	21.8	14%	21.2
	$\Delta\theta_b$	18.3	22.5	22.6	25.5	22.1	24.5	30.4	26.6	19.6	22.8	29.0	-	24.0	15%	21.5
	+	43.1	41.2	43.3	48.8	45.1	50.3	47.2	51.3	41.8	45.4	46.5	-	45.8	7%	42.7
5	$\Delta\theta_d$	22.6	23.8	30.9	24.2	19.1	19.6	22.1	21.8	24.6	29.6	24.9	-	23.9	15%	20.2
	$\Delta\theta_b$	22.7	20.4	26.2	19.6	29.8	24.8	19.8	44.3	26.7	28.7	22.2	-	26.0	27%	19.6
	+	45.3	44.2	57.1	43.8	48.9	44.4	41.9	66.1	51.3	58.3	47.1	-	49.9	15%	39.8
6	$\Delta\theta_d$	24.3	30.2	23.4	20.8	23.6	23.5	21.2	23.8	24.9	25.4	24.8	26.1	24.3	10%	20.6
	$\Delta\theta_b$	19.5	31.6	17.2	30.4	32.8	28.9	25.6	20.4	26.2	25.1	18.3	23.8	25.0	21%	18.8
	+	43.8	61.8	40.6	51.2	56.4	52.4	46.8	44.2	51.1	50.5	43.1	49.9	49.3	12%	39.4

TABLE 4. Summary of angles corresponding to data in Figure 4*

Cycle No.	$\Delta\theta_d$	$\Delta\theta_b$	$\Delta\theta_{0.1}$	$\Delta\theta_{0.1\text{-}0.9}$	$\Delta\theta_t$	"b"
1**	20.9 (0.94)	22.2	20.6 (0.93)	22.5 (1.01)	56. (2.52)	0.40
2	20.9 (1.15)	18.2	19.8 (1.09)	18.0 (0.99)	50. (2.75)	0.47
3	20.5 (0.89)	23.0	22.5 (0.98)	21.8 (0.95)	54. (2.35)	0.39
4	19.1 (0.64)	29.9	22.9 (0.77)	28.8 (0.96)	64. (2.14)	0.30
5	20.8 (1.13)	18.4	21.1 (1.15)	18.3 (0.99)	50. (2.72)	0.46
6	19.0 (0.87)	21.9	21.0 (0.96)	20.9 (0.95)	54. (2.47)	0.38
7	24.9 (1.12)	22.3	24.3 (1.09)	22.4 (1.00)	60. (2.69)	0.46
8	28.1 (1.01)	27.8	23.9 (0.86)	25.3 (0.91)	62. (2.23)	0.43
9	32.4 (1.40)	23.1	30.0 (1.30)	23.4 (1.01)	68. (2.94)	0.55
10	20.0 (0.83)	24.1	21.2 (0.88)	25.6 (1.06)	62. (2.57)	0.37
Average	22.9 (1.00) [0.99]	22.6	23.0 (1.01) [1.05]	22.7 (0.98) [1.02]	58.2 (2.54) [2.53]	0.42
Rel. Var.	20% (21%)	16%	13% (16%)	15% (4%)	11% (10%)	17%

*Units: θ in crank-angle degrees; $\bar{u}_e$ in m/s.

**First cycle not considered in averages.

TABLE 5.

Statistics of $\bar{u}_e$, $u_b = (R + r_s)6N/\Delta\theta_b$ in m/s
and $\tau_d = \Delta\theta_d/6N$, $\tau_i = (\theta_i - \theta_s)/6N$ in ms

Run No.		Cycle No.														
		2	3	4	5	6	7	8	9	10	11	12	13	Avg	Rel. Var.	First Cycle
1	u_e	9.0	10.6	8.4	9.1	-	-	-	-	-	-	-	-	9.3	10%	8.4
	u_b	17.5	21.1	23.5	18.5	21.7	16.2	18.2	14.8	20.2	-	-	-	19.1	15%	20.6
	τ_d	3.83	4.21	3.66	4.35	3.91	2.89	3.54	4.18	3.75	-	-	-	3.81	12%	2.28
	τ_i	1.26	0.68	0.73	0.62	-	-	-	-	-	-	-	-	0.82	36%	0.59
2	u_e	8.4	9.5	8.0	6.6	9.0	8.8	11.8	12.5	11.9	-	-	-	9.6	21%	9.5
	u_b	15.0	20.9	20.6	17.2	14.4	14.2	22.5	21.5	18.2	-	-	-	18.3	18%	21.7
	τ_d	4.02	4.13	5.39	4.04	5.18	3.88	4.59	4.51	3.52	-	-	-	4.36	14%	2.62
	τ_i	1.10	0.87	0.79	0.52	0.80	1.32	1.11	1.40	0.63	-	-	-	0.95	32%	1.05
3	u_e	8.2	8.3	7.5	8.4	14.5	10.6	14.2	13.0	12.5	-	-	-	10.8	26%	8.4
	u_b	29.1	23.0	17.7	28.8	24.2	23.8	19.1	22.9	22.0	-	-	-	23.4	15%	23.9
	τ_d	3.17	3.11	2.89	3.15	2.88	3.77	4.26	4.91	3.03	-	-	-	3.46	20%	3.17
	τ_i	0.82	0.81	0.77	0.86	0.83	0.76	0.55	1.05	0.72	-	-	-	0.80	17%	0.66
4	u_e	7.2	14.8	14.8	13.0	12.8	9.6	9.5	12.1	14.2	13.8	9.1	-	11.9	22%	9.1
	u_b	29.5	24.0	23.9	21.2	24.4	22.0	17.8	20.3	27.5	23.7	18.6	-	23.0	15%	25.1
	τ_d	3.69	2.78	3.08	3.47	3.42	3.84	2.50	3.68	3.30	3.36	2.60	-	3.25	14%	3.15
	τ_i	0.58	0.37	0.29	0.32	0.77	0.52	1.03	0.44	0.00	0.82	0.71	-	0.53	55%	0.54
5	u_e	9.7	9.6	10.8	9.2	9.9	10.3	15.6	8.5	12.2	-	-	-	10.6	20%	12.6
	u_b	25.9	28.8	22.4	30.0	19.7	23.7	29.7	13.3	22.0	20.5	26.5	-	23.9	21%	30.0
	τ_d	3.09	3.25	4.22	3.31	2.61	2.68	3.02	2.98	3.36	4.04	3.40	-	3.72	15%	2.76
	τ_i	1.44	0.68	0.80	0.47	1.00	0.46	0.86	0.62	0.69	-	-	-	0.78	39%	0.58
6	u_e	17.5	9.4	15.3	11.7	11.0	11.9	14.5	9.3	10.7	11.7	10.2	15.5	12.4	21%	12.3
	u_b	30.4	18.8	34.5	19.5	18.1	20.5	23.1	29.0	22.6	23.6	32.4	24.9	24.8	21%	31.5
	τ_d	3.29	4.09	3.17	2.82	3.20	3.18	2.87	3.22	3.37	3.44	3.36	3.54	3.30	10%	2.79
	τ_i	0.81	1.28	0.46	1.80	0.78	0.82	0.97	0.18	0.91	0.86	0.47	1.13	0.87	48%	0.51

TABLE 6.

Entrainment speed, comparison with other parameters

and Blizard and Keck's results

		Present Work	Blizard & Keck
Engine speed, rev/min	N	1000	1000
Piston face inlet valve area ratio	A_p/A_i	5.7	8.4
Mean piston speed, m/s	$\bar{u}_p$	3.0	2.6
Mean inlet gas speed, m/s	$\bar{u}_i$	17	21
Entrainment speed, m/s	u_e	10	6
Ratio	$u_e/\bar{u}_p$	3.3	2.3
Ratio	$u_e/\bar{u}_i$	0.59	0.28

TABLE A. Characteristic length scales

Quantity	Symbol	Units	"a"	"b"
pressure	p	MPa	2	4
unburnt gas temperature	T_u	K	800	920
integral length scale	ℓ	mm	13	14
turbulence intensity	u'	m/s	10	10
dynamic viscosity	μ	mPa•s	342	378
unburnt gas density	ρ_u	kg/m^3	9.2	16
kinematic viscosity	ν	mm^2/s	3.7	2.4
turbulent Reynolds number	Re_ℓ		35000	58000
Taylor microscale	λ	mm	0.48	0.40
microscale Reynolds number	Re_λ		1300	1670
Kolmogorov microscale	η	μm	6.8	5.0
Kolmogorov time scale	τ_η	μs	12	10
characteristic burning time	τ	ms	1.5	0.9
laminar flame speed	S_ℓ	m/s	1.0	1.5
laminar burning length scale	ℓ_ℓ	mm	1.5	1.3
entrainment speed	u_e	m/s	10	10
flame "thickness"	ℓ_f	mm	15	9
time after IVC	$\bar{t}$	ms	20	23
diffusion length	δ	mm	0.28	0.23
laminar flame thickness	δ_ℓ	μm	5.4	2.1
wall quench distance	δ_q	μm	70	40

List of Figures

List of Figures (continued)

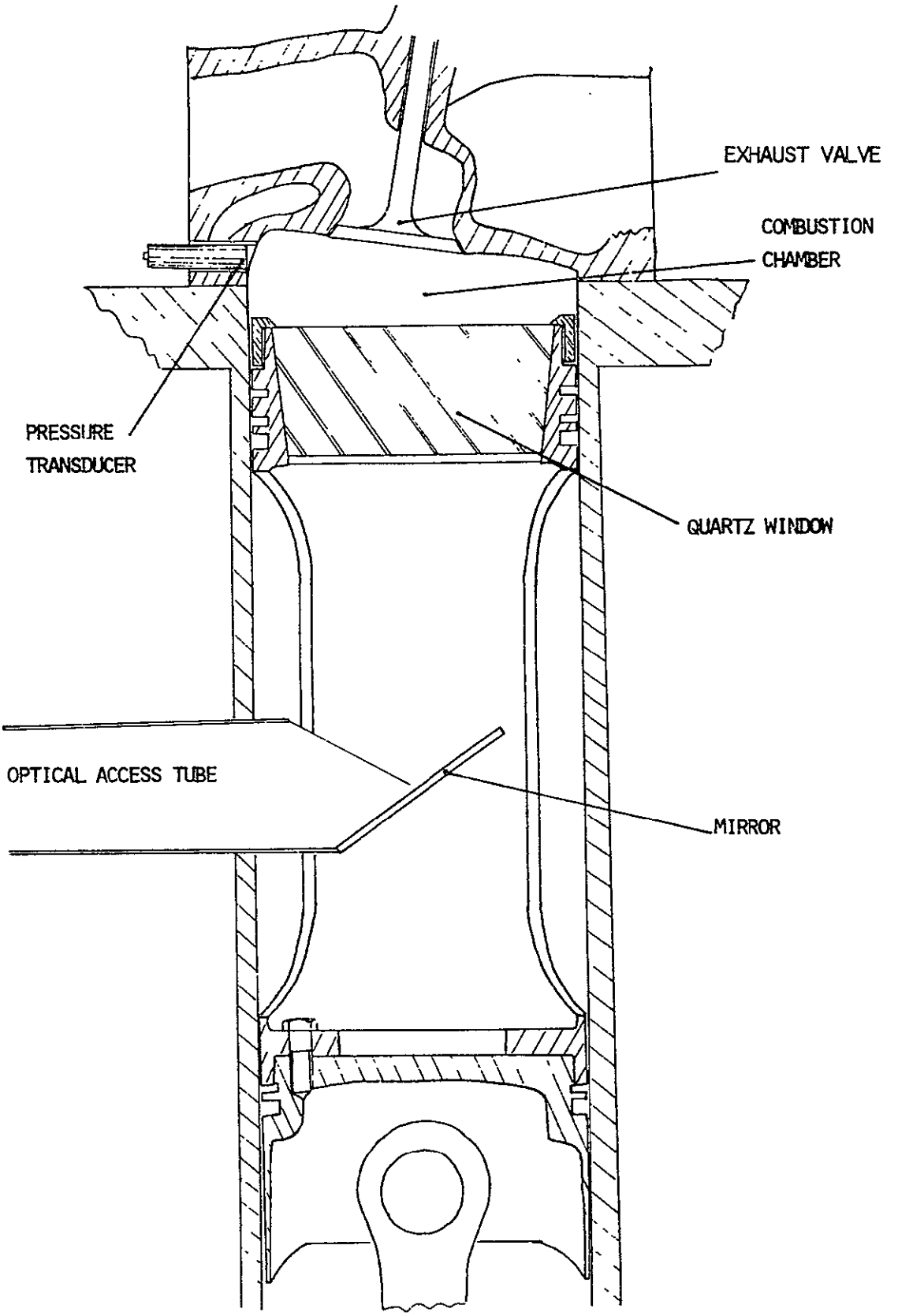

Figure 1. Engine setup

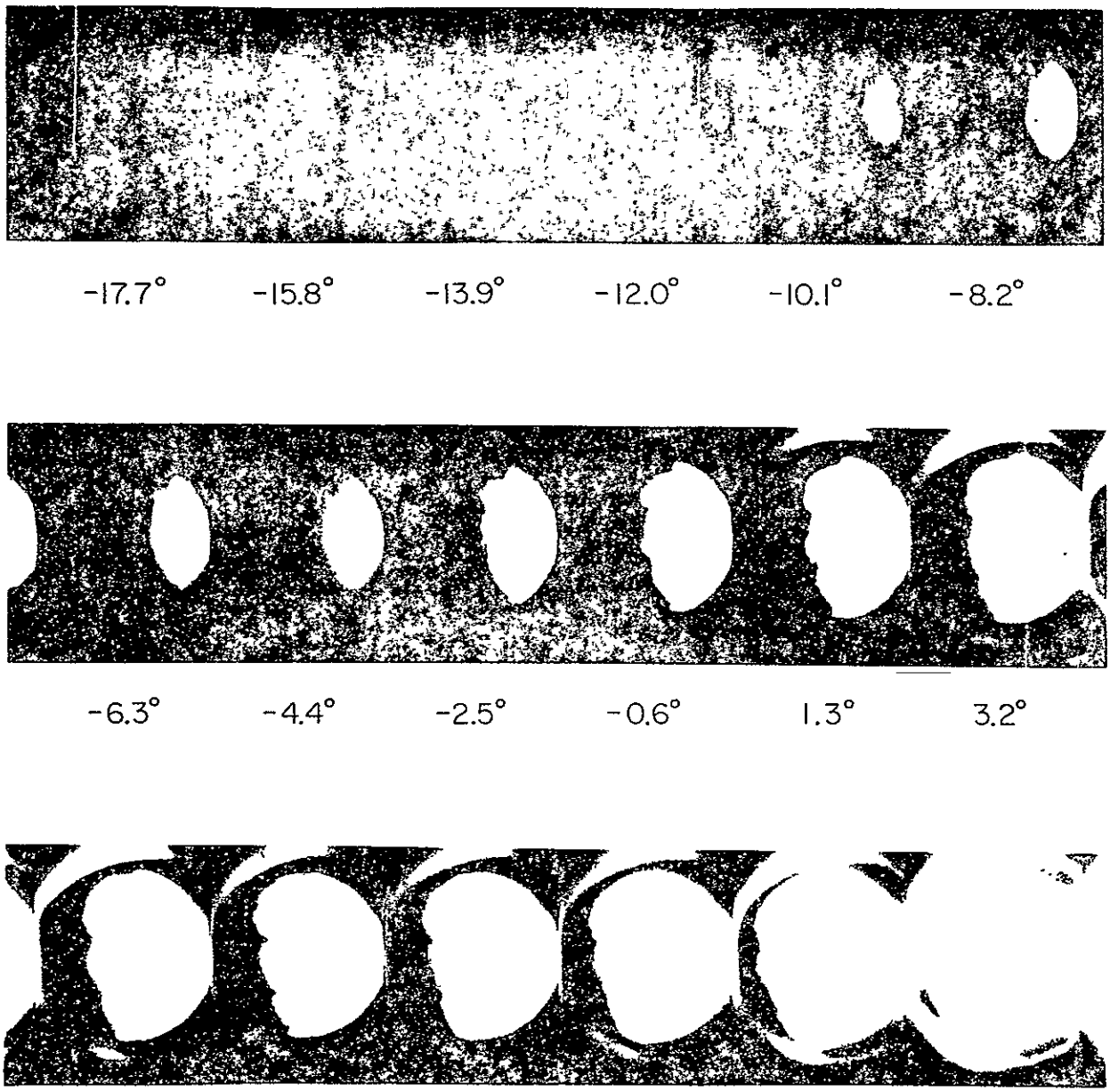

Figure 2. Pressure vs. crank-angle θ for the typical sequence of cycles.

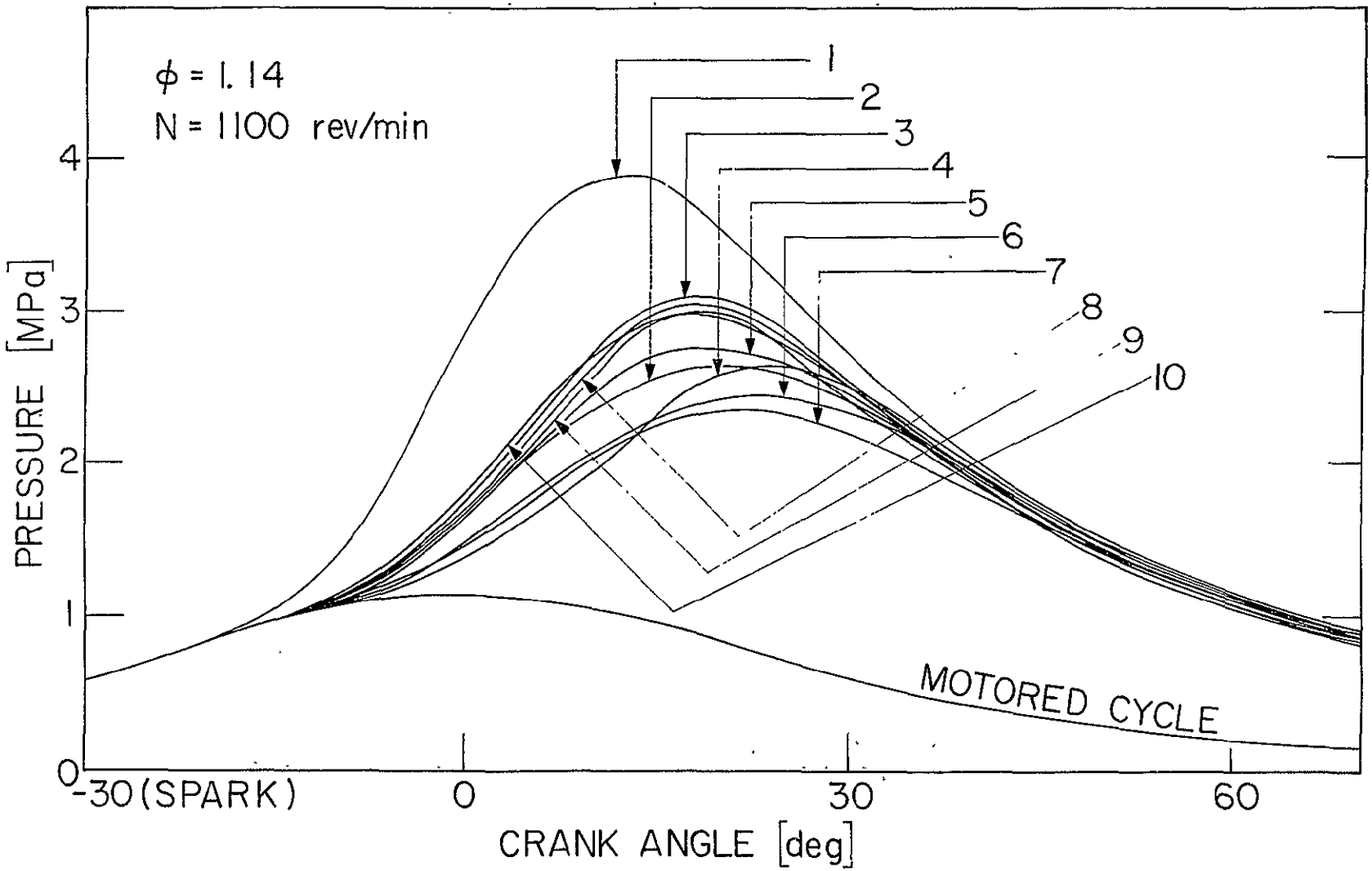

Figure 3. Typical photographic sequence corresponding to pressure curve number 9 of Figure 2.

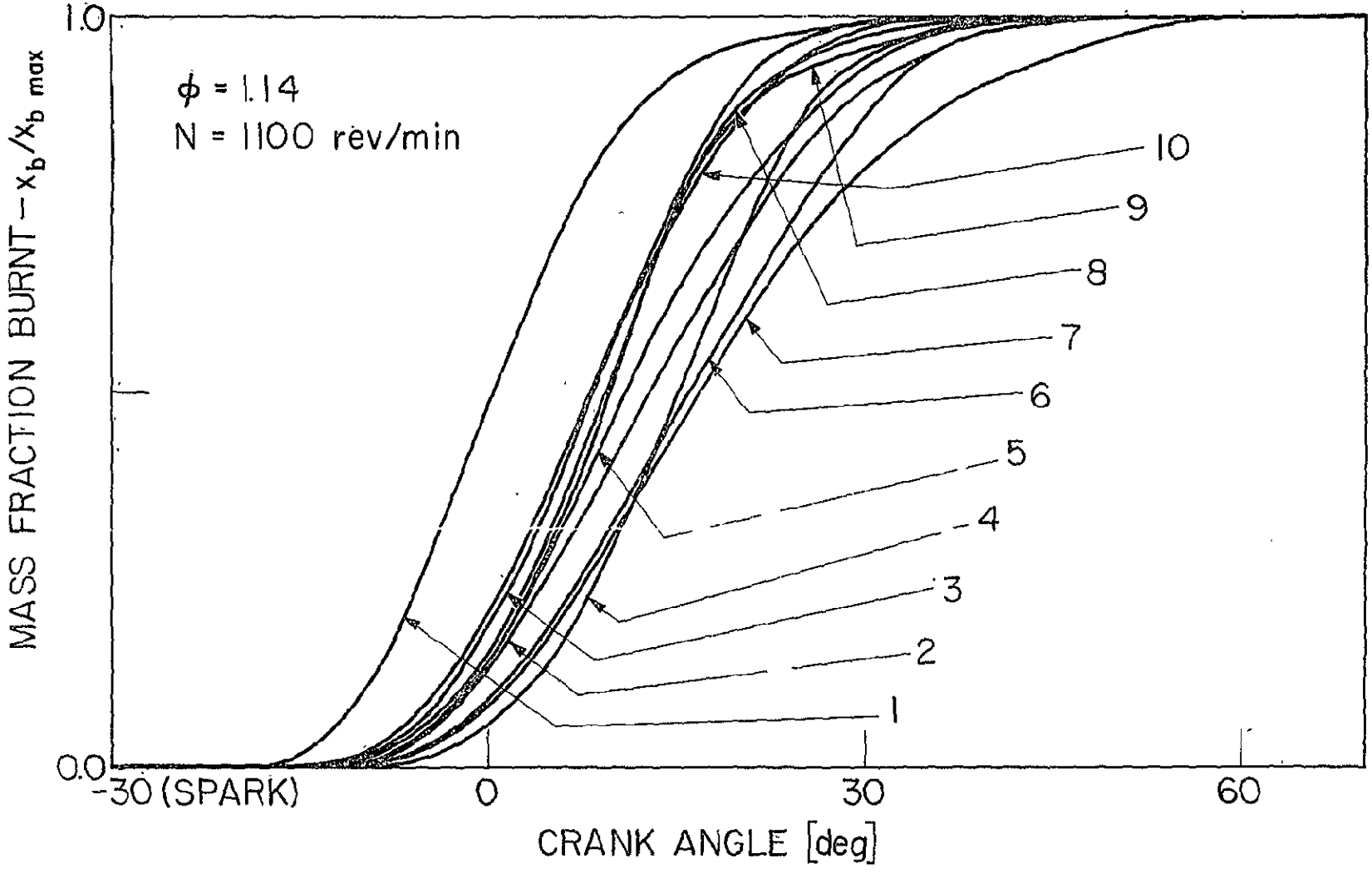

Figure 4. Normalized mass fraction burnt $\eta = x_b/x_{b\ max}$ vs. θ for pressure curves in Figure 2.

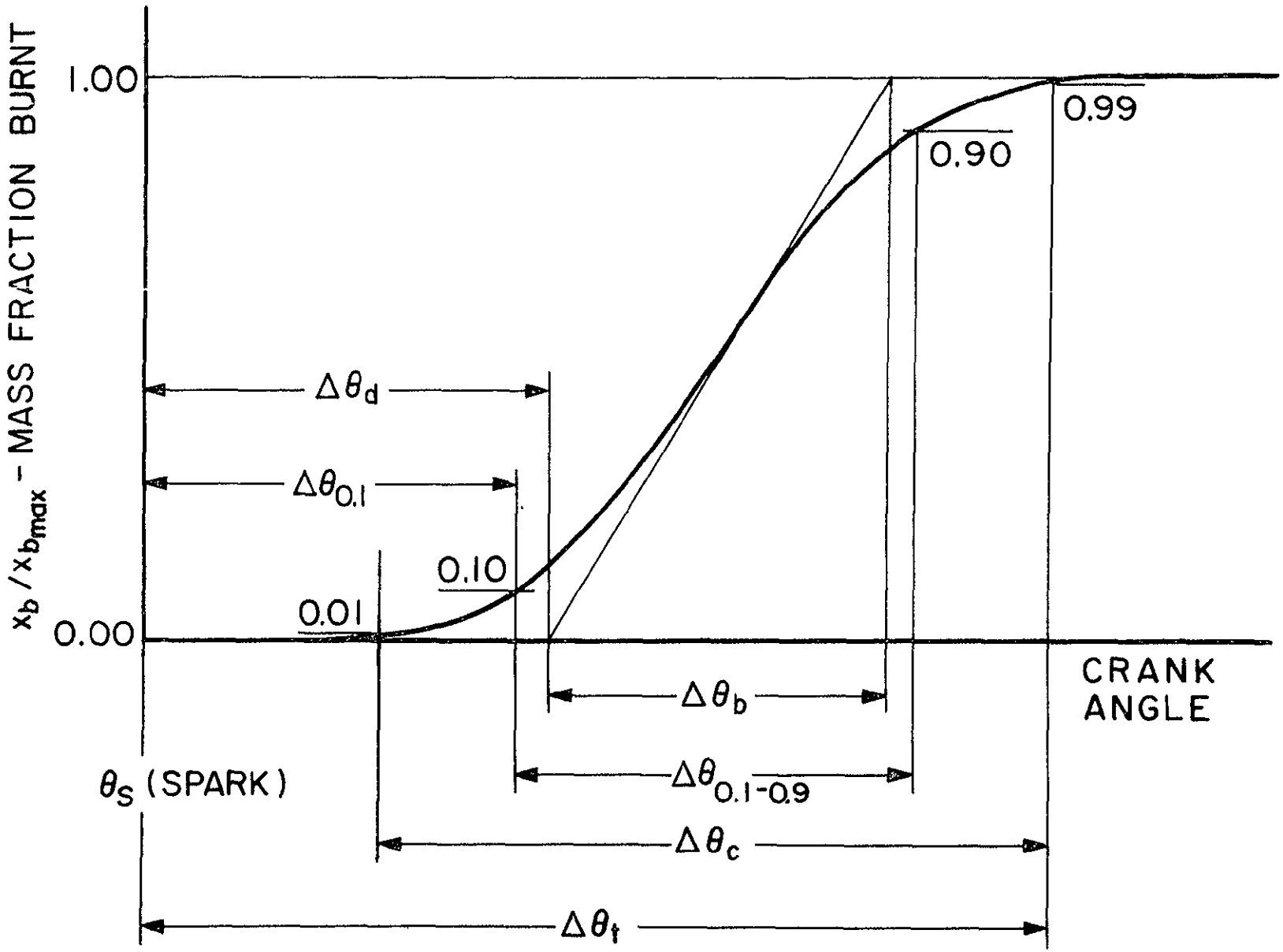

Figure 5. Definition of characteristic angles.

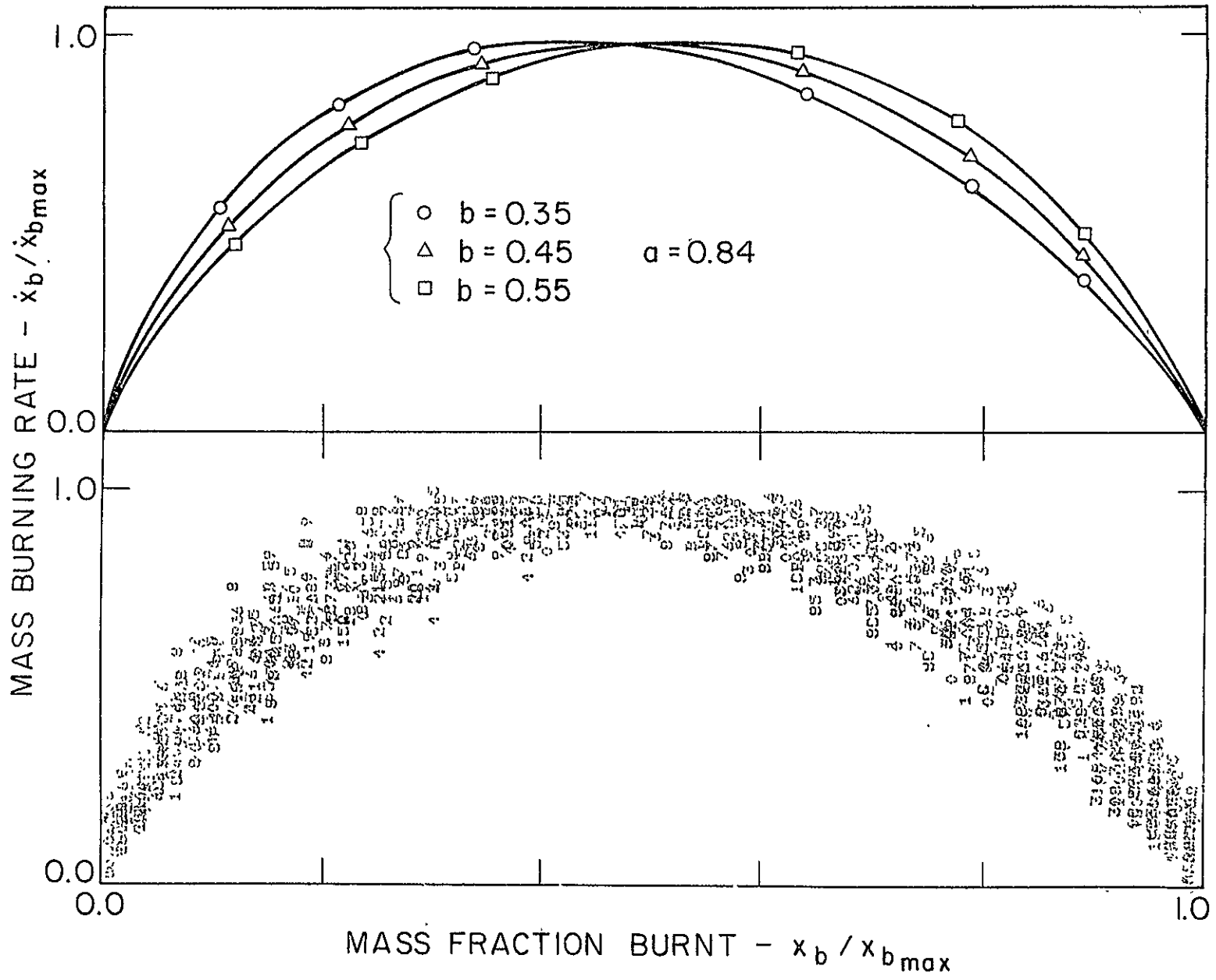

Figure 6. $f(\eta) = \dot{x}_b/\dot{x}_{b\ max}$ vs. $\eta = x_b/x_{b\ max}$.

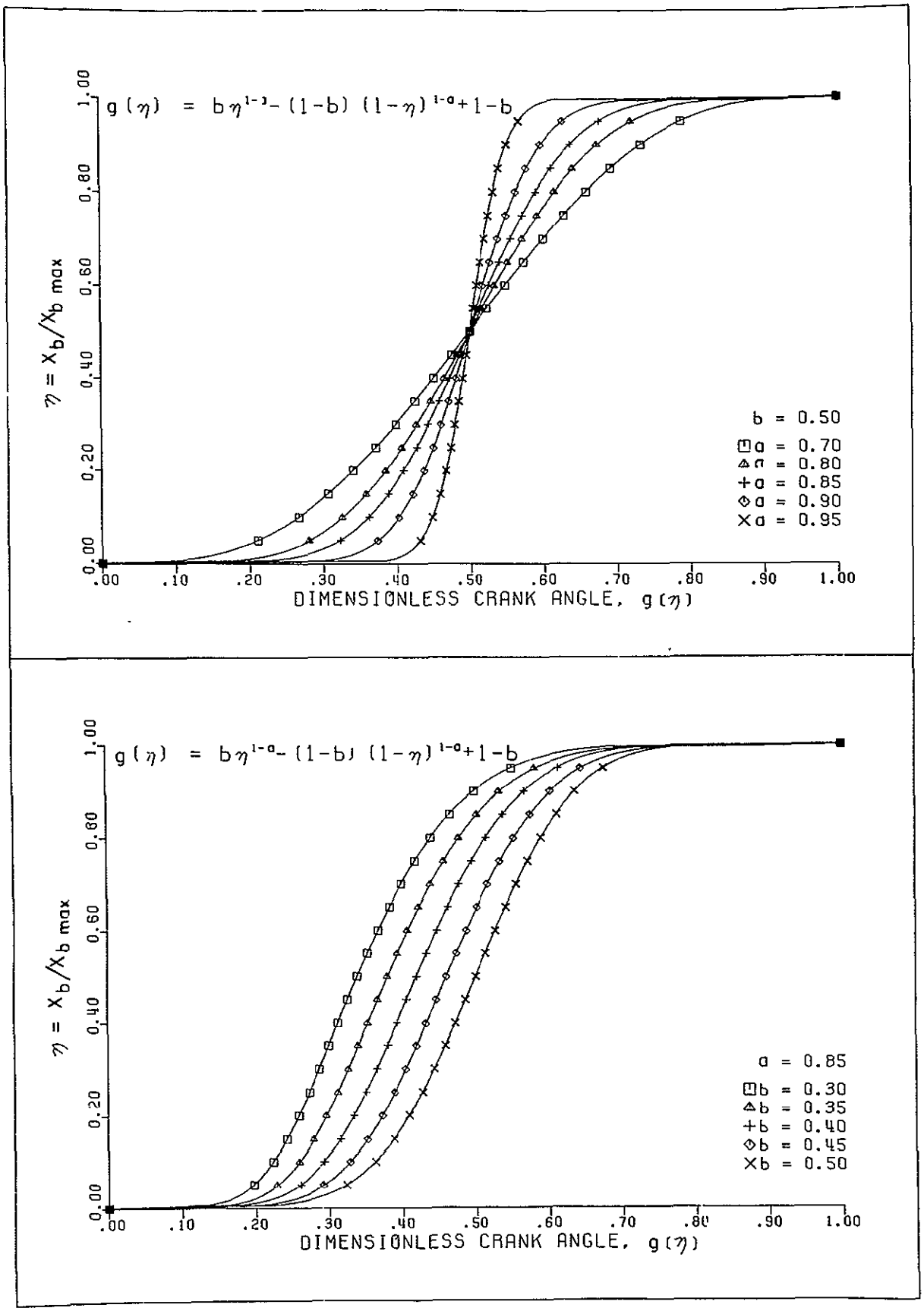

Figure 7. Effect of parameters on the empirical burning law.

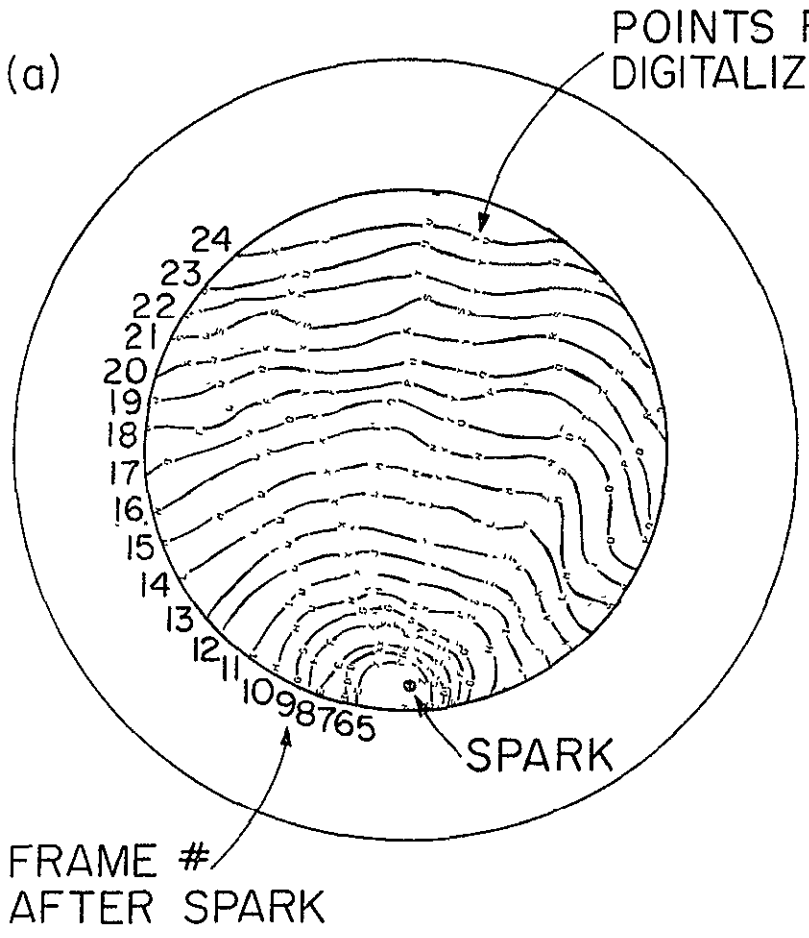

Figure 8a. Flame front profiles for the typical pressure curve number 9 in Fig. 2

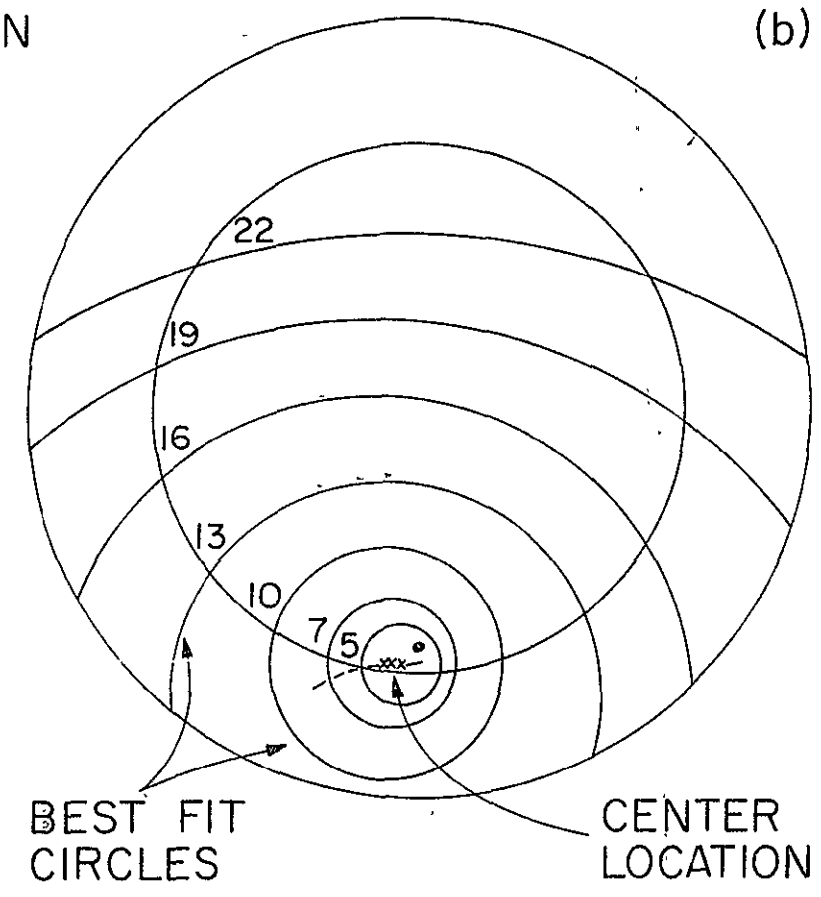

Figure 8b. Best fit circles and locus of center for contours in Fig. 8a.

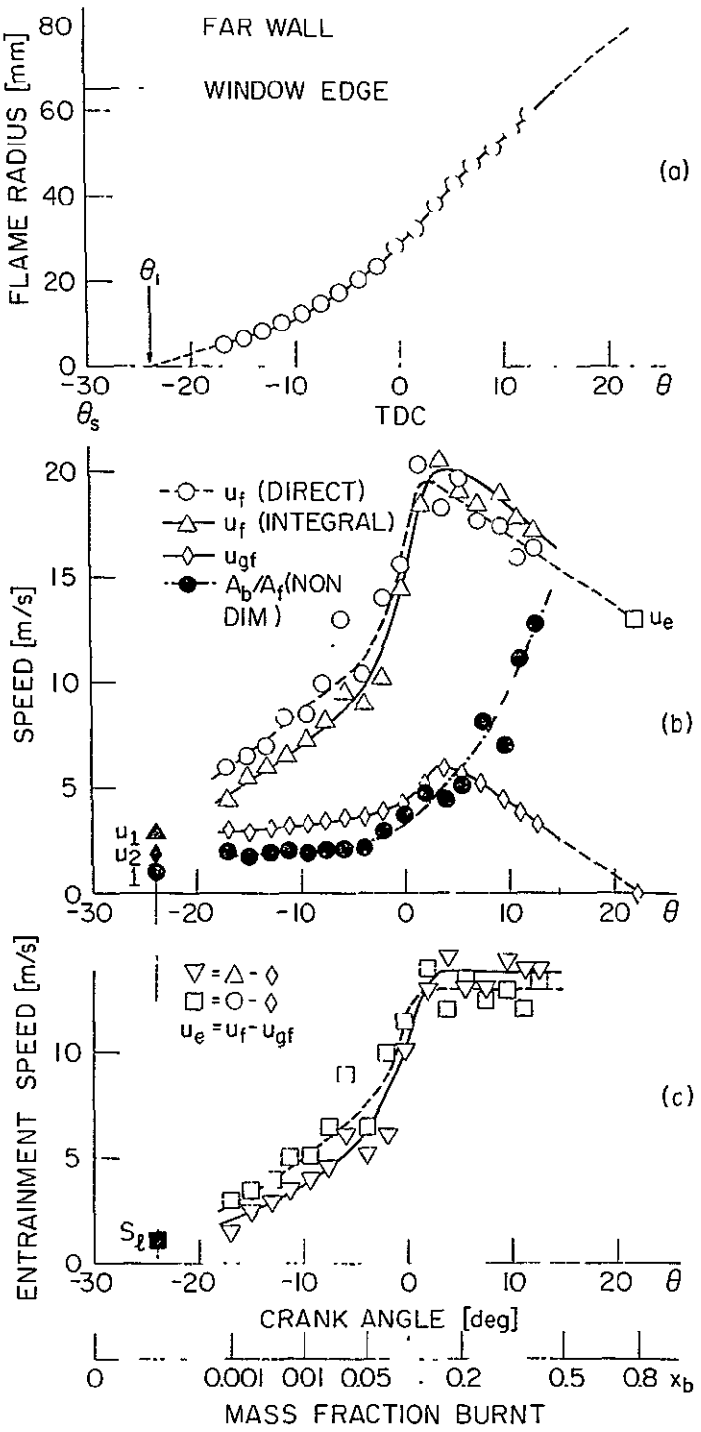

Figure 9a. Flame radius $r_f + x_c - x_s$ vs. crank-angle θ for the typical contours in Fig. 8a.

Figure 9b. Flame front speed u_f evaluated with both direct and integral method and gas speed u_{gf} vs. crank-angle for the same cycle. The flame stretch factor A_b/A_f is also shown.

Figure 9c. Entrainment speed u_e vs. crank-angle.

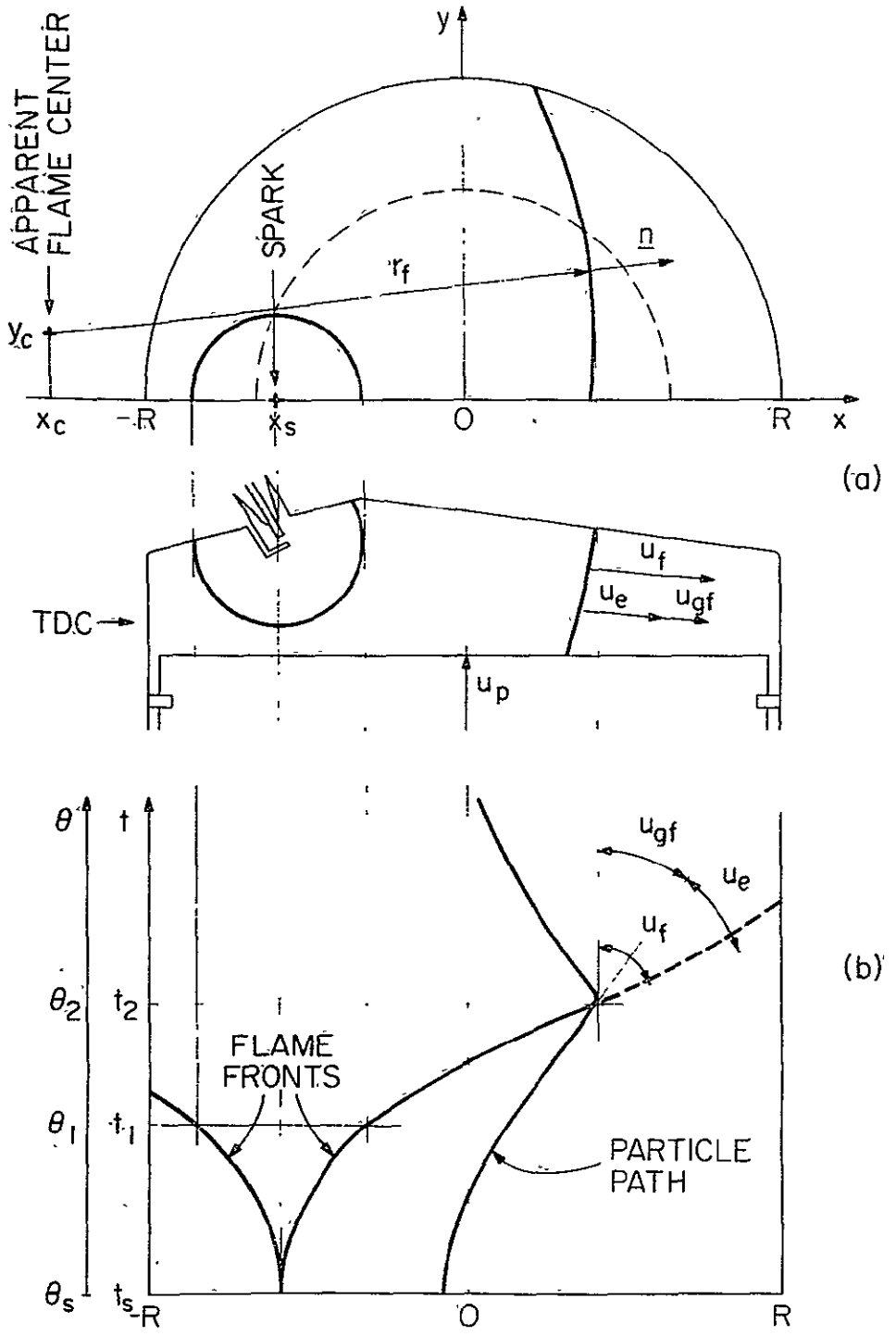

Figure 10a. Cylinder head geometry and assumed best spherical flame fronts for an early and a late visible contours.

Figure 10b. Crank-angle or time vs. distance plot showing typical flame front and gas particle average paths. A geometrical visualization of u_f, u_{gf} and u_e is also given.

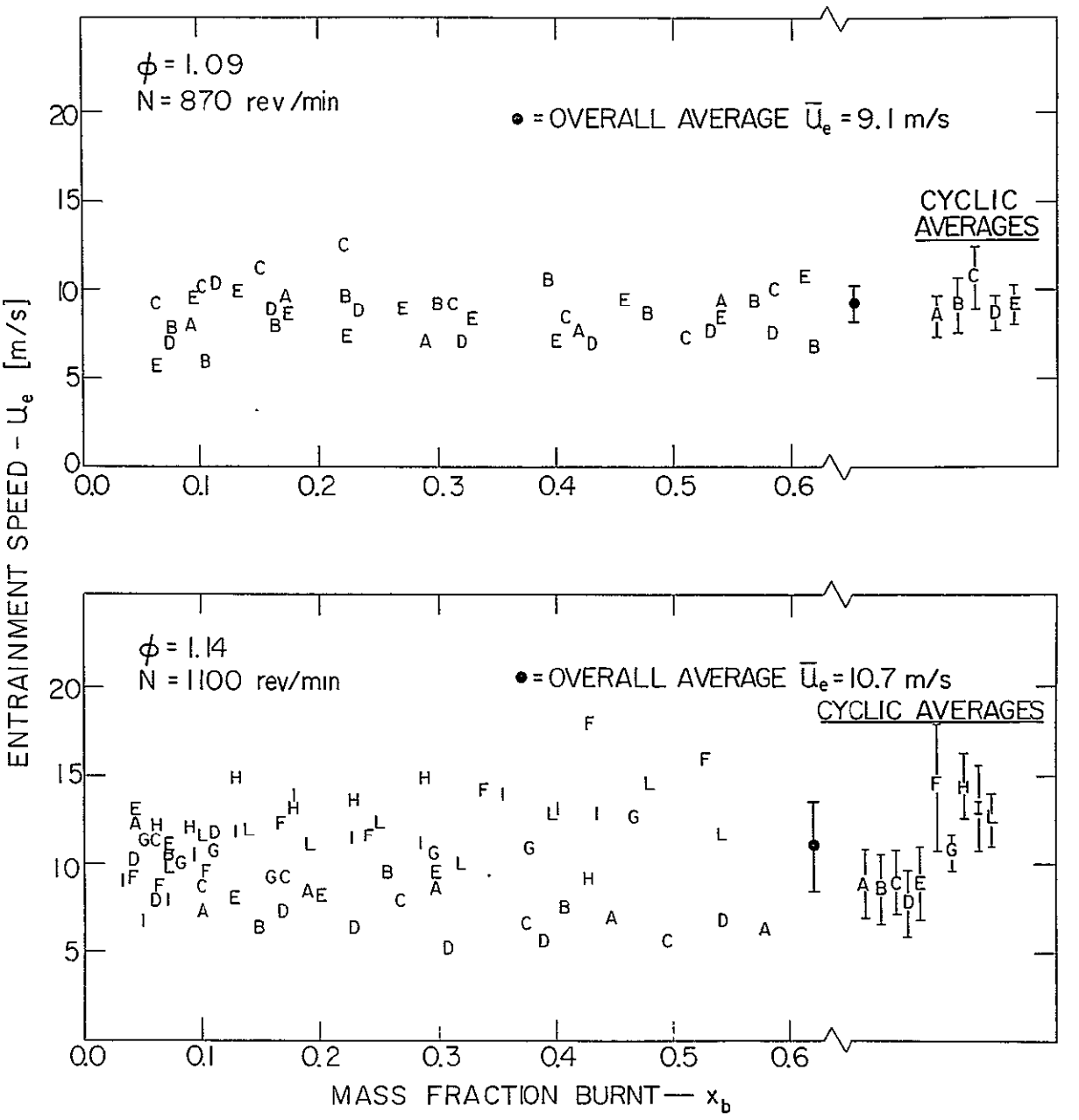

Figure 11. Entrainment speed u_e vs. x_b for two typical sequences.

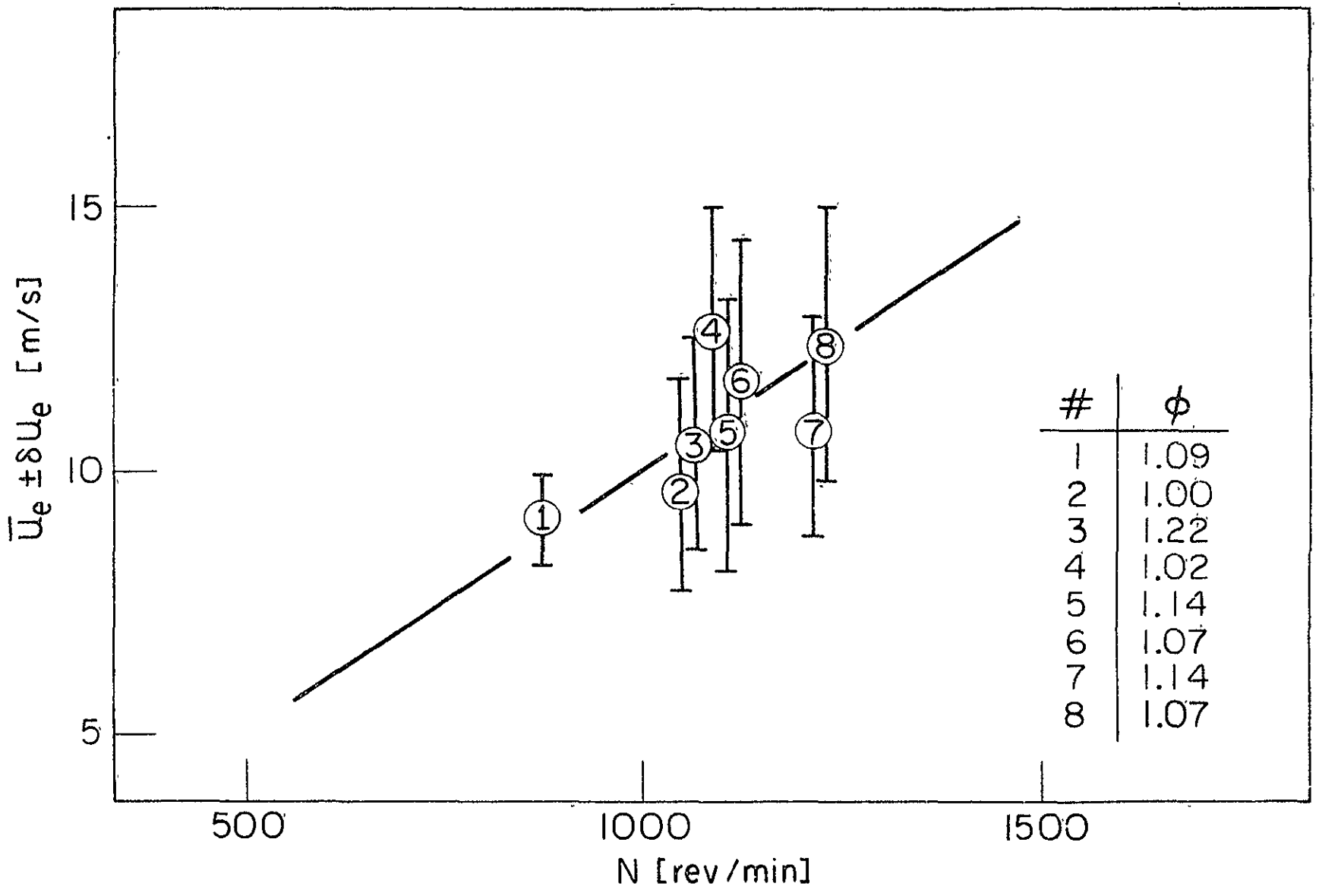

Figure 12. Entrainment speed $\bar{u}_e$ vs. engine speed N.

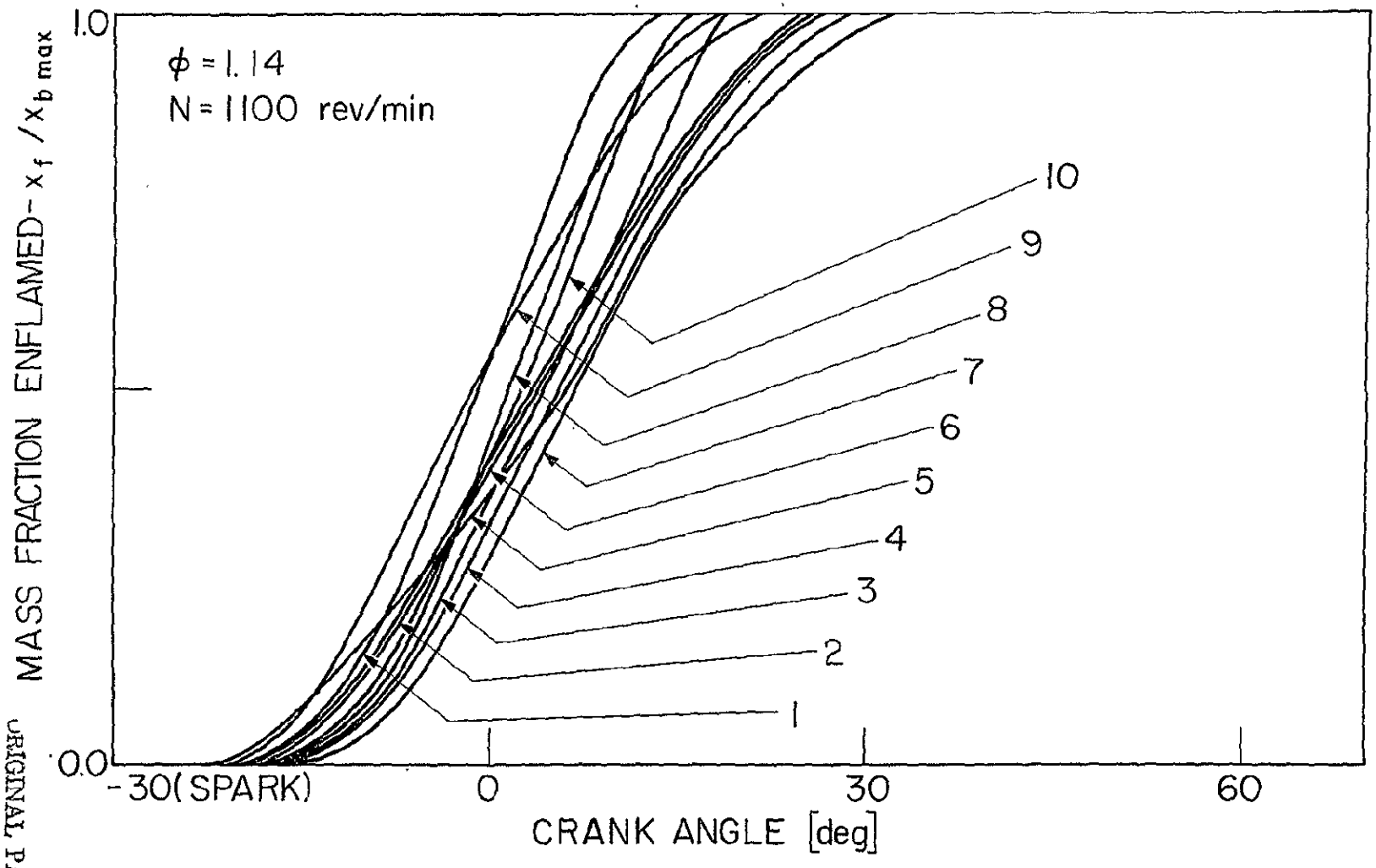

Figure 13. Normalized mass fraction enflamed curves for the sequence of Figure 2 to 4.

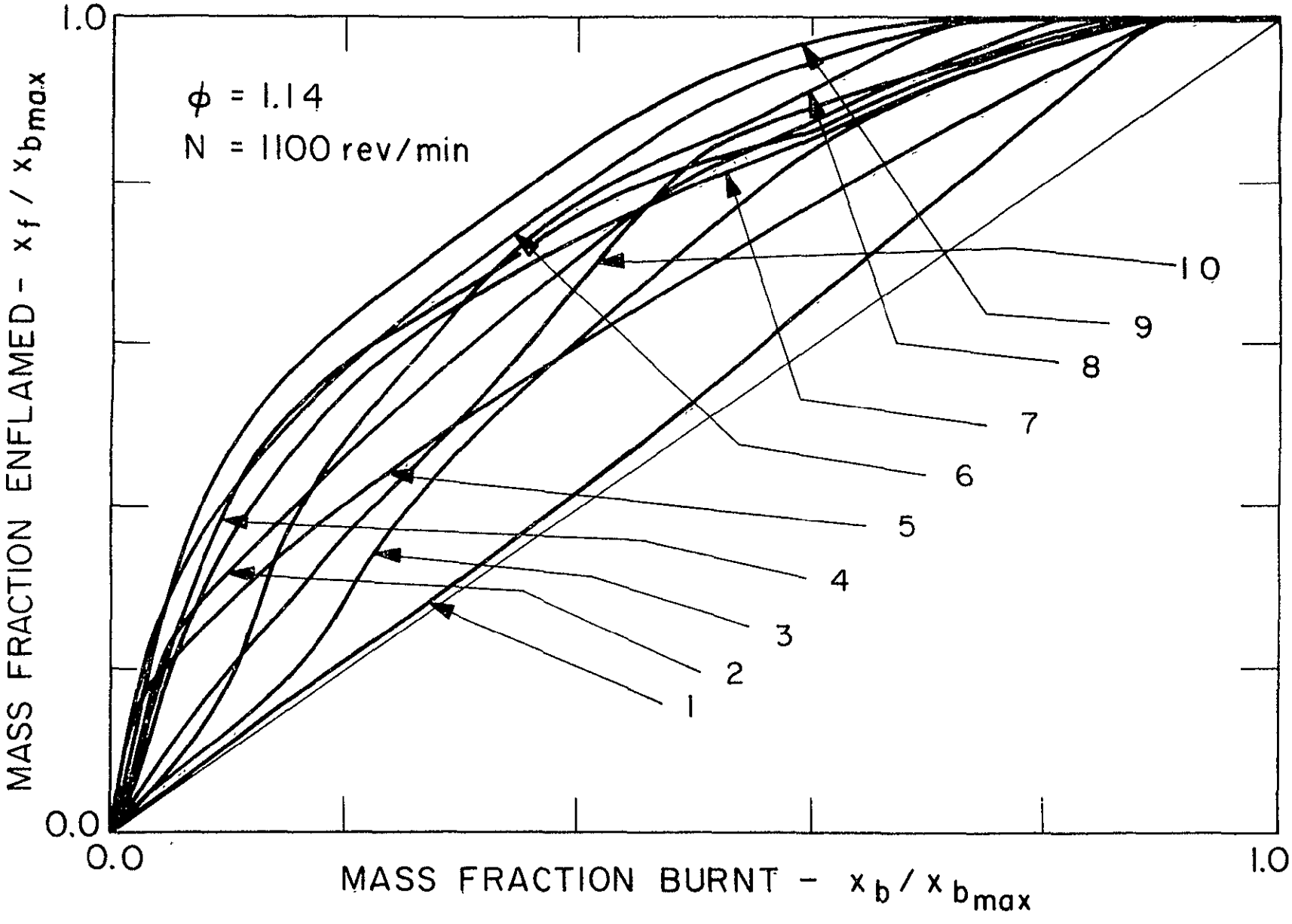

Figure 14. Enflamed vs. burnt mass fractions for the same sequence of Figure 13.

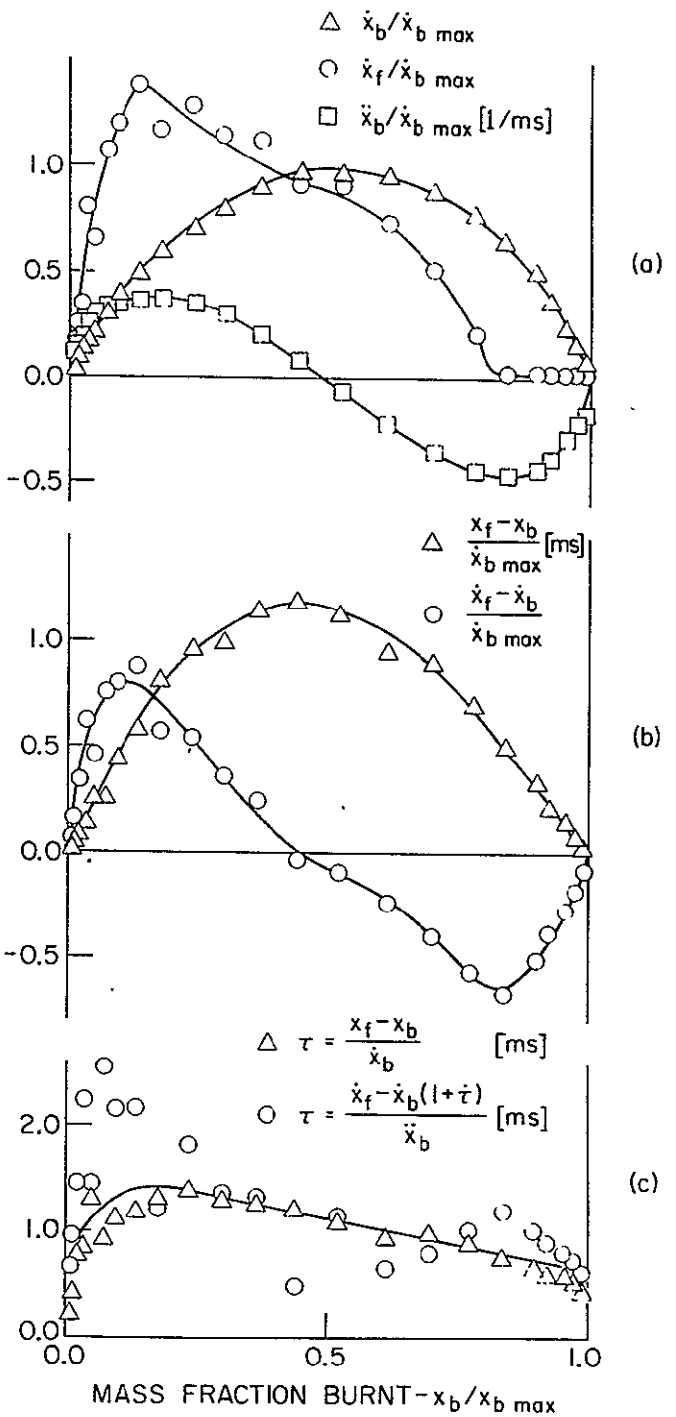

Figure 15a. Normalized rates of entrainment $\dot{x}_f/\dot{x}_{b\,max}$ and burning $\dot{x}_b/\dot{x}_{b\,max}$ for the typical cycle of Fig. 8. The second time derivative $\ddot{x}_b/\dot{x}_{b\,max}$ has units of 1/ms.

Figure 15b. Normalized difference between enflamed and burnt mass fractions $(x_f-x_b)/\dot{x}_{b\,max}$ in ms and normalized difference between entrainment and burning rates $(\dot{x}_f-\dot{x}_b)/\dot{x}_{b\,max}$.

Figure 15c. Characteristic burning time τ vs. $x_b/x_{b\,max}$ calculated with two different methods for the typical cycle.